AD-A102 555 NAVAL RESEARCH LAB WASHINGTON DC F/G 4/1
NONLINEAR EQUATORIAL SPREAD F: THE EFFECT OF NEUTRAL WINDS AND --ETC(U)
JUL 81 S T ZALESAK, S L OSSAKOW
UNCLASSIFIED NRL-MR-4588 NL

1 OF 1
AD A
102555

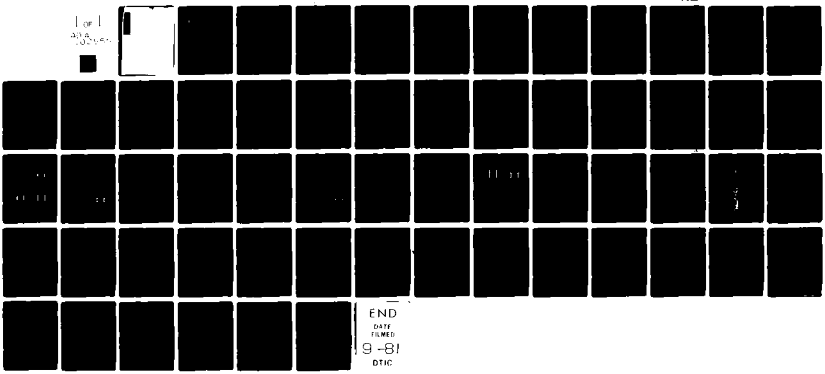

END
DATE
FILMED
9-81
DTIC

(14) NRL-MR-4588

(9) REPORT DOCUMENTATION PAGE		READ INSTRUCTIONS BEFORE COMPLETING FORM
1. REPORT NUMBER NRL Memorandum Report 4588	2. GOVT ACCESSION NO. AD-A102 555	3. RECIPIENT'S CATALOG NUMBER
4. TITLE (and Subtitle) (6) NONLINEAR EQUATORIAL SPREAD F: THE EFFECT OF NEUTRAL WINDS AND BACKGROUND PEDERSEN CONDUCTIVITY		5. TYPE OF REPORT & PERIOD COVERED Interim report on a continuing NRL problem.
		6. PERFORMING ORG. REPORT NUMBER
7. AUTHOR(s) (10) S.T. Zalesak, S.L. Ossakow ~~and~~ P.K. Chaturvedi*		8. CONTRACT OR GRANT NUMBER(s) (16) RR033302
9. PERFORMING ORGANIZATION NAME AND ADDRESS Naval Research Laboratory Washington, D.C. 20375 (12) 58		10. PROGRAM ELEMENT, PROJECT, TASK AREA & WORK UNIT NUMBERS (17) 61153N; RR0330244; 47-0883-01; 62704H; 47-0889-01
11. CONTROLLING OFFICE NAME AND ADDRESS Defense Nuclear Agency, Washington, D.C. 20305 Office of Naval Research, Arlington, VA 22217		12. REPORT DATE July 29, 1981
		13. NUMBER OF PAGES 60
14. MONITORING AGENCY NAME & ADDRESS (if different from Controlling Office) (11) 29 Jul 81		15. SECURITY CLASS. (of this report) UNCLASSIFIED
		15a. DECLASSIFICATION/DOWNGRADING SCHEDULE

16. DISTRIBUTION STATEMENT (of this Report)

Approved for public release; distribution unlimited.

17. DISTRIBUTION STATEMENT (of the abstract entered in Block 20, if different from Report)

18. SUPPLEMENTARY NOTES

*Present address: Berkeley Research Associates, Springfield, VA 22150.

This research was sponsored partially by the Defense Nuclear Agency under Subtask S99QAXHC, work unit 00002, and work unit title, "Plasma Structure Evolution," and partially by the Office of Naval Research.

19. KEY WORDS (Continue on reverse side if necessary and identify by block number)

Nonlinear equatorial spread F
Numerical simulations
Neutral winds
Background Pedersen conductivity
Bubble tilts

20. ABSTRACT (Continue on reverse side if necessary and identify by block number)

A simple model of the interaction of the equatorial ionosphere with the eastward F region neutral wind in the presence of evolving spread F bubbles or plumes is given. A consequence of the model is that the upper portions of plumes will take on a westward tilt, while the lower portions will tilt eastward, giving rise to the "fishtails" and "C's" observed by coherent backscatter radar measurements of field aligned small scale irregularities. The essence of the model is that the plasma away from the equatorial plane

(Continues)

251950

20. ABSTRACT (Continued)

(e.g., a background nighttime E region at higher latitudes) makes a finite contribution to the magnetic field line integrated Pedersen conductivity, causing an incomplete coupling of the plasma motion to the neutral wind. The degree of coupling is then a function of the Pedersen conductivities both near the equator in the F region and in the higher latitude E region, giving rise to vertical shears of east-west plasma motion having opposing signs on either side of the equatorial Pedersen conductivity maximum. Evolving spread F plumes are caught up in this shear as they rise vertically, resulting in the characteristic "C" shape seen by backscatter radar, and in the westward motion of plasma bubbles observed by satellite in situ measurements. Numerical simulations, incorporating an eastward neutral wind in the equatorial F region and E region Pedersen conductivity effects, are presented to further support the model and analysis. The simulations also show the result that it may be the eastward as well as the westward wall of the plume which is subject to secondary instabilities in the presence of an eastward neutral wind. In addition, even without the neutral wind, the numerical simulations show that E region Pedersen conductivity effects can result in a slowing down of equatorial spread F and attendant bubble evolution.

CONTENTS

NONLINEAR EQUATORIAL SPREAF F:
THE EFFECT OF NEUTRAL WINDS AND
BACKGROUND PEDERSEN CONDUCTIVITY

1. Introduction

In our previous studies of evolving equatorial spread F (ESF) bubbles and plumes in the equatorial ionosphere [Scannapieco and Ossakow, 1976; Ossakow et al., 1979; Zalesak and Ossakow, 1980], the effects of the neutral wind were neglected. Rather, we focused our attention on showing that the motion and structure of the experimentally measured ESF environment (bottomside and topside spread F, bubble formation and evolution) could be explained in terms of the nonlinear evolution of the gravitationally driven collisional Rayleigh-Taylor instability. Through the use of numerical simulation techniques we were able to demonstrate both qualitative and quantitative agreement with the observations. We wished to show that a simple model (i.e., using only gravity and the bottomside background electron density gradient as drivers), followed into the nonlinear regime, could explain observations that were up to that point inexplicable. However, there are some aspects of the observations which we do not see in our previous simulations.

First, there is the tendency of ESF structure to drift eastward at approximately the neutral wind velocity, obviously something which could not be duplicated in a numerical simulation which neglected neutral wind effects. Secondly, there is the curious tendency on the part of radar backscatter maps of ESF to show plumes of backscatter intensity which tilt eastward with altitude at the lower altitudes and westward with altitude at the higher altitudes. These structures were dubbed "C's" and "fishtails" by

Manuscript submitted June 9, 1981.

Woodman and La Hoz [1976] and have also been seen in the ALTAIR backscatter maps of Tsunoda [1981], although Tsunoda chooses not to regard the eastward-tilting and westward-tilting structures as part of the same plume. Additionally, we should point out that McClure et al., [1977] have observed the westward drift of plasma bubbles (bite-outs or depletions). We propose here a simple model of the interaction of the eastward neutral wind at the equator with the equatorial ionosphere which we believe explains both of these observations. At this juncture, we should point out that Woodman and La Hoz [1976] , Ott [1978], and Ossakow and Chaturvedi [1978] hypothesized that an eastward neutral wind would produce a westward drift of ESF bubbles.

Briefly, we find that if the magnetic field line integrated Pedersen conductivity has a finite contribution from plasma which is not subject to the equatorial F region neutral wind (e.g., plasma at higher latitude E regions), then the vertical polarization electric field driven by the neutral wind at the equator is partially shorted out by this "background" E region conductivity, causing there to be relative motion, or "slip", between the plasma and the neutral wind at the equator. This effect was first described by Rishbeth [1971] . Further investigation shows that the degree of "slip" is inversely proportional to the "local" (i.e., equatorial F region) Pedersen conductivity, causing there to be a vertical shear in the plasma motion even when there is no vertical shear in the neutral wind. This plasma shear bends any vertical structure about the "local" maximum in Pedersen conductivity, giving rise to the "C's" and "fishtails" seen on coherent backscatter radar maps (Woodman and La Hoz, 1976; Tsunoda, 1981). Zalesak et al. (1980) have presented a preliminary version of this model.

In section 2 we present the geometry of the physical problem we are modeling and briefly review the relevant equations of motion. We also show

that any passive structure placed in the ambient equatorial environment will, in fact, be bent into C-shaped structures. However, spread F plumes are far from passive structures, and it is necessary to perform nonlinear numerical simulations to prove the case unequivocally. These simulations are presented in section 3, where we also show the surprising result that, for the case studied, it may be the <u>eastward</u> wall of the plume, as well as the westward wall, which is subject to secondary instabilities. A stability analysis which included only the interaction of the neutral wind with the plasma gradients in the bubble would conclude that it should be only the westward wall of the plume which is unstable. Consideration of the self-consistent polarization electric field of the bubble itself, as well as of gravitational effects on the tilted structure can cause the instability to "switch sides". In section 4 we present our conclusions, and in section 5 we discuss briefly our plans for future work.

2. Theory

In Figure 1, we show the geometry of the physical phenomenon we are attempting to model. The equatorial F region plasma responds to the effects of the earth's magnetic field, gravity, collisions with the neutral atmosphere, and electric fields. Since the conductivity along magnetic field lines is extremely high, these electric fields can depend on the dynamics of plasma far from the equatorial region, but connected to the equatorial region by magnetic field lines. We find that the physical quantity dominating the evolution of the collisional Rayleigh-Taylor instability is the magnetic field line integrated Pedersen conductivity, and that the primary contribution to that quantity comes from plasma in the local region near the "computational plane" shown in Figure 1. This fact has been the basis for our previous theoretical and numerical studies of equatorial spread F, (Scannapieco and Ossakow, 1976; Ossakow et al., 1979; Zalesak and Ossakow, 1980) and has enabled us to study the phenomena of interest using just a single two-dimensional computational plane.

We do not propose here to analyze the problem in the complete three-dimensional geometry, but rather, as a first step, to modify our two-dimensional model to take into account the presence of other plasma, and hence Pedersen conductivities and forces, in regions far from the equatorial plane, but connected to the equatorial F region plasma along magnetic field lines. For instance this could be the northern and southern hemisphere E region plasma shown in Figure 1. This modification is shown in Figure 2, where we show three distinct layers of plasma connected by magnetic field lines. The center layer is the same computational plane as we have used in our previous work (Scannapieco and Ossakow, 1976; Ossakow et al., 1979;

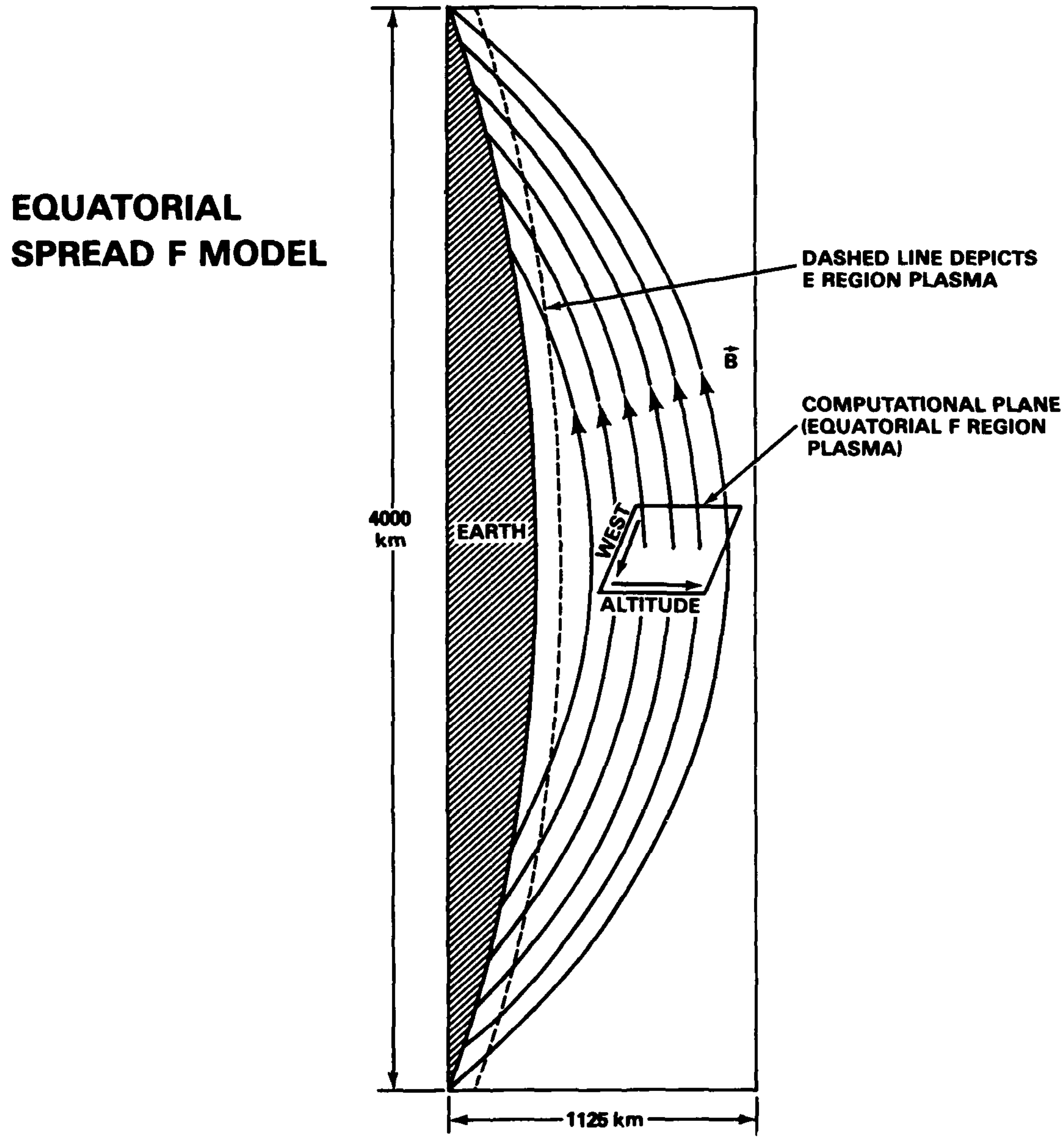

Fig. 1 — Diagram of the equatorial ionosphere and of the neighboring regions which have physical relevance to equatorial spread F (ESF) processes, including the E region plasma at higher and lower latitudes. These regions are electrically coupled to the equatorial F region ionosphere by the high conductivity along magnetic field lines. Plasma is actually distributed all along these field lines, but in this study we shall make the assumption that this system can be modeled accurately by three planes of plasma connected by straight field lines, as shown in Figure 2. One of these three layers (layer 2 in Figure 2) is shown here as the "computational plane."

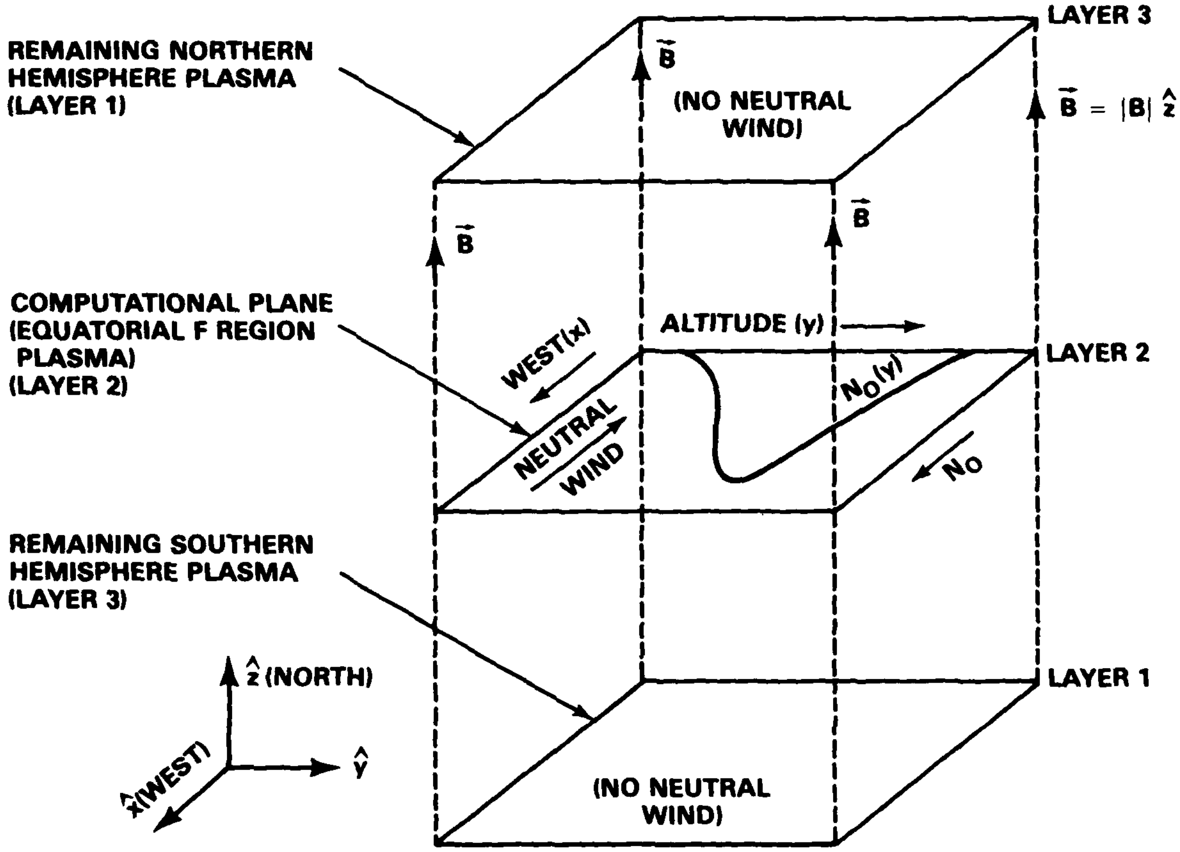

Fig. 2 — The "three layer" model of the physical system depicted in Figure 1. All plasma in the vicinity of the equatorial plane has been compressed into layer 2, while the remaining northern and southern hemisphere plasma has been compressed into layers 1 and 3 respectively. Further, the magnetic field lines have been straightened so we can deal in cartesian coordinates x, y, and z as shown in the figure. The plasma in layers 1 and 3 is assumed to be uniform and free of any external driving force such as a neutral wind. The equatorial layer 2 is assigned a realistic initial distribution of electron density $N_0(y)$, and ion-neutral collision frequency, along with a neutral wind which may vary with altitude, but which is taken to be uniform and eastward, and equal to 150 m/sec in this study. In addition, gravity points in the negative y direction.

Zalesak and Ossakow, 1980) and represents the equatorial nighttime F region plasma. The upper and lower layers represent the remaining northern and southern hemisphere plasma respectively, including the E region plasma. The problem is still essentially two-dimensional in that we do not allow transport of ions between layers, nor do we allow any physical quantity to vary with z within a layer, where z is the direction along the magnetic field. We do, however, allow electron currents to flow along field lines between the layers to preserve electrical neutrality. Also, within the context of this model, we will finally take the E region layers to act as a passive load, i.e., we do not allow for any change in layers 1 and 3 and those layers are assumed to remain uniform. Thus, as a first cut we are taking our previous equatorial plane simulations (Scannapieco and Ossakow, 1976; Ossakow et al., 1979; Zalesak and Ossakow, 1980) and adding a passive E region load to the circuit to allow for short circuiting effects. Under the assumptions that: (i) the electric fields of interest are electrostatic and, hence, derivable from a scalar potential; and (ii) the conductivity along magnetic field lines is extremely large and, hence, the potential is constant along a field line, we are left with a problem similar to the multilevel barium cloud striation problem [Lloyd and Haerendal, 1973; Scannapieco et al., 1974; 1976; Doles et al., 1976]. We will now briefly derive the multilevel equations, in general form, appropriate to our ESF problem.

Consider a plasma consisting of ions and electrons imbedded in a magnetic field aligned along the z axis. The continuity and momentum equations describing the system are:

$$\frac{\partial n_\alpha}{\partial t} + \nabla \cdot (n \underline{v}_\alpha) = - \nu_R n_\alpha \qquad (1)$$

$$\left(\frac{\partial}{\partial t} + \underline{v}_\alpha \cdot \nabla\right)\underline{v}_\alpha = \frac{q_\alpha}{m_\alpha}\left(\underline{E} + \frac{\underline{v}_\alpha \times \underline{B}}{c}\right) + \underline{g} - \nu_{\alpha n}\,(\underline{v}_\alpha - \underline{U}_n) \tag{2}$$

where the subscript α denotes the species (i for ions, e for electrons), n is the species number density, $\underline{v}$ is velocity, ν_R is the recombination coefficient, $\underline{E}$ is the electric field, $\underline{g}$ is the gravitational acceleration, q is the species charge, $\nu_{\alpha n}$ is the species collision frequency with the neutral atmosphere, $\underline{U}_n$ is the neutral wind velocity, c is the speed of light, and m is the species mass. Note that we have neglected finite temperature effects (pressure), and the effects of ion-ion collisions and electron-ion collisions (eventually, we will even neglect electron-neutral collisions). We further assume that we are interested only in average drift velocities over time scales long compared to either the mean time between collisions or the gyroperiod. In this case we can neglect the inertial terms (the left hand side) of (2), and invert the equation to obtain an algebraic expression for $\underline{v}_\alpha$:

$$\underline{v}_{\alpha\perp} = k_{1\alpha}\,\underline{F}_{\alpha\perp} + k_{2\alpha}\,\underline{F}_{\alpha\perp} \times \hat{z} \tag{3}$$

$$\underline{v}_{\alpha\parallel} = k_{o\alpha}\,\underline{F}_{\parallel} \tag{4}$$

where

$$k_{1\alpha} = \frac{\nu_{\alpha n}}{\Omega_\alpha}\;\frac{c}{|q_\alpha B|}\left[1 - \frac{(\nu_{\alpha n}/\Omega_\alpha)^2}{1 + (\nu_{\alpha n}/\Omega_\alpha)^2}\right] \tag{5}$$

$$k_{2\alpha} = \frac{c}{q_\alpha B}\left[1 - \frac{(\nu_{\alpha n}/\Omega_\alpha)^2}{1 + (\nu_{\alpha n}/\Omega_\alpha)^2}\right] \tag{6}$$

$$k_{o\alpha} = (m_\alpha \nu_{\alpha n})^{-1} \tag{7}$$

$$\underline{F}_\alpha = q_\alpha\,\underline{E} + m_\alpha\,\underline{g} + \nu_{\alpha n}\,m_\alpha \underline{U}_n \tag{8}$$

$$\hat{z} \equiv \underline{B}/|B| \tag{9}$$

$$\Omega_\alpha \equiv \left|\frac{q_\alpha B}{m_\alpha c}\right| \tag{10}$$

The vector subscripts $\perp$ and $\|$ refer to the components of the vector which are perpendicular and parallel respectively to $\hat{z}$. We take $q_i = e$ and $q_e = -e$. We then assume that $\nu_{en}/\Omega_e \approx 0$ and obtain

$$k_{1i} = \frac{\nu_{in}}{\Omega_i} R_i \frac{c}{e|B|} \tag{11}$$

$$k_{1e} = 0 \tag{12}$$

$$k_{2i} = R_i \frac{c}{eB} \tag{13}$$

$$k_{2e} = -\frac{c}{eB} \tag{14}$$

$$R_i = (1 + \nu_{in}{}^2/\Omega_i{}^2)^{-1} \tag{15}$$

We now define the perpendicular current

$$\underline{j}_\perp = \sum_\alpha n_\alpha q_\alpha \underline{v}_{\alpha\perp} \tag{16}$$

Substituting (11) through (15), (3) and (4) into (16), and using the quasi-neutrality approximation

$$n_i \approx n_e \equiv n \tag{17}$$

we obtain

$$\underline{j}_\perp = \frac{\nu_{in}}{\Omega_i} R_i \frac{n c}{|B|} \underline{F}_{i\perp} + \frac{nc}{B} (R_i \underline{F}_{i\perp} + \underline{F}_{e\perp}) \times \hat{z} \tag{18}$$

For our problem

$$\underline{F}_{i\perp} = e\,\underline{E}_{\perp} + m_i\,\underline{g}_{\perp} + \nu_{in}\,m_i\,\underline{U}_{n\perp} \tag{19}$$

$$\underline{F}_{e\perp} = -\,e\,\underline{E}_{\perp} + m_e\,\underline{g}_{\perp} \tag{20}$$

and we obtain

$$\underline{j}_{\perp} = \frac{\nu_{in}}{\Omega_i}\,R_i\,\frac{nc}{|B|}\,(e\,\underline{E}_{\perp} + m_i\,\underline{g}_{\perp} + \nu_{in}\,m_i\,\underline{U}_{n\perp})$$

$$+R_i\,\frac{nc}{B}\left[e\,\underline{E}_{\perp}\,(1-R_i^{-1}) + (m_i + \frac{m_e}{R_i})\,\underline{g}_{\perp} + \nu_{in}\,m_i\,\underline{U}_{n\perp}\right] \times \hat{z} \tag{21}$$

Since $0.01 \leq R_i \leq 1.0$ we may neglect m_e/R_i with respect to m_i.

Defining the Pedersen conductivity

$$\sigma_p \equiv R_i\,\frac{\nu_{in}}{\Omega_i}\,\frac{nce}{|B|} \tag{22}$$

and noting that $1-R_i^{-1} = -\,\nu_{in}^{\;2}/\Omega_i^{\;2}$ we obtain

$$\underline{j}_{\perp} = \sigma_p \left[\underline{E}_{\perp} + \frac{m_i}{e}\,\underline{g}_{\perp} + \nu_{in}\,\frac{m_i}{e}\,\underline{U}_{n\perp} + \left(-\frac{\nu_{in}}{\Omega_i}\,\underline{E}_{\perp} + \frac{\Omega_i m_i}{\nu_{in} e}\,\underline{g}_{\perp} + \Omega_i\,\frac{m_i}{e}\,\underline{U}_{n\perp}\right) \times \hat{z}\right] \tag{23}$$

Equation (23) is to be applied to each of our layers of plasma. Referring to Figures 1 and 2 we see that for layers 1 and 3 $\underline{U}_n = 0$ and further that $\underline{g}_{\perp} = -\,Dgy$ where $g = 980\ \mathrm{cm/sec^2}$ and $0<D<1$ to account for the fact that $\underline{g}$ is not perpendicular to $\underline{B}$ for plasma away from the equatorial plane (D is actually $\cos\theta_D$ where θ_D is the dip angle). Under the assumptions we shall make later it will be seen that the value of D is irrelevant and can be taken to be zero. In layer 2, the equatorial plane, we have $\underline{g}_{\perp} = -\,g\,\hat{y}$, and we make the assumption that the neutral wind is directed along the $\hat{x}$ axis ($\underline{U} = U_n\,\hat{x}$, where $\hat{x}$ points west). Furthermore, since layer 2 is taken to be at F region altitudes where $\nu_{in}/\Omega_i \ll 1$ ($R_i \approx 1$), we can neglect in that layer

the second, third, and fourth terms of equation (23) with respect to the fifth, sixth, and first, respectively. So we have for the three layers:

$$\underline{j}_{\perp 1} = \sigma_{p1}\left[\underline{E}_{\perp} - \left(\frac{\Omega_i m_i}{\nu_{in} e} Dg + \frac{\nu_{in}}{\Omega_i} E_y\right)\hat{x} - \left(\frac{m_i}{e} Dg - \frac{\nu_{in}}{\Omega_i} E_x\right)\hat{y}\right]_1 \tag{24}$$

$$\underline{j}_{\perp 3} = \sigma_{p3}\left[\underline{E}_{\perp} - \left(\frac{\Omega_i m_i}{\nu_{in} e} Dg + \frac{\nu_{in}}{\Omega_i} E_y\right)\hat{x} - \left(\frac{m_i}{e} Dg - \frac{\nu_{in}}{\Omega_i} E_x\right)\hat{y}\right]_3 \tag{25}$$

$$\underline{j}_{\perp 2} = \sigma_{p2}\left[\underline{E}_{\perp} - \frac{\Omega_i m_i}{\nu_{in} e} g\hat{x} - \Omega_i \frac{m_i}{e} U_n \hat{y}\right]_2 \tag{26}$$

where the numerical subscripts refer to the layer numbers depicted in Figure 2.

Quasi-neutrality demands that

$$\underline{\nabla} \cdot \underline{j} = \frac{\partial}{\partial x} j_x + \frac{\partial}{\partial y} j_y + \frac{\partial}{\partial z} j_z = 0 \tag{27}$$

Integrating (27) along field lines and assuming that j_z vanishes at $z = \pm\infty$ we obtain

$$\int_{-\infty}^{+\infty} \nabla_{\perp} \cdot j_{\perp} \, dz = 0 \tag{28}$$

where

$$\nabla_{\perp} \equiv \hat{x}\frac{\partial}{\partial x} + \hat{y}\frac{\partial}{\partial y} \tag{29}$$

If we model our plasma as an array of discrete layers of planes of plasma perpendicular to the magnetic field as in Figure 2 we may replace the integral by a sum:

$$\sum_{k=1}^{3} \nabla_\perp \cdot \underline{j}_{\perp k} \quad \Delta z_k = 0 \tag{30}$$

where Δz_k is the thickness of layer k measured along the magnetic field line. By our assumption of equipotential magnetic field lines and electrostatic electric fields

$$\underline{E}_{\perp 1} (x,y) = \underline{E}_{\perp 2} (x,y) = \underline{E}_{\perp 3} (x,y) = \underline{E} (x,y) = - \nabla_\perp \phi (x,y) \tag{31}$$

where we have neglected the slight convergence of the magnetic field. Then (30) becomes

$$\begin{aligned} \nabla_\perp \quad & \left[(\Sigma_{p1} + \Sigma_{p2} + \Sigma_{p3}) \quad \nabla_\perp \phi \right] + H = \\ & - \frac{\partial}{\partial x} \left(\Sigma_p \frac{\Omega i}{\nu_{in}} \quad \frac{m_i g}{e} \right)_2 - \frac{\partial}{\partial y} \left(\Sigma_p \Omega_i \quad \frac{m_i U_n}{e} \right)_2 \\ & - \frac{\partial}{\partial x} \left(\Sigma_p \frac{\Omega_i}{\nu_{in}} \quad \frac{m_i Dg}{e} \right)_b \quad - \frac{\partial}{\partial y} \left(\Sigma_p \frac{m_i Dg}{e} \right)_b \quad , \end{aligned} \tag{32}$$

where the subscript b denotes the sum of levels 1 and 3 and

$$\Sigma_{pk} = \int_{\text{layer } k} \sigma_p \quad dz \approx \sigma_{pk} \Delta z_k \tag{33}$$

Also we have defined

$$H \equiv -\frac{\partial}{\partial x}\left(\frac{\nu_{in}}{\Omega_i}\ \Sigma_p\ \frac{\partial\phi}{\partial y}\right)_b + \frac{\partial}{\partial y}\left(\Sigma_p\ \frac{\nu_{in}}{\Omega_i}\ \frac{\partial\phi}{\partial x}\right)_b$$

$$= -\frac{\partial\phi}{\partial y}\ \frac{\partial}{\partial x}\left(\frac{\nu_{in}}{\Omega_i}\ \Sigma_p\right)_b + \frac{\partial\phi}{\partial x}\ \frac{\partial}{\partial y}\left(\frac{\nu_{in}}{\Omega_i}\ \Sigma_p\right)_b \tag{34}$$

Note that implicit in the above manipulation is the assumption that σ_p and ν_{in}/Ω_i are constant along a magnetic field line within a given layer, as we had assumed earlier. Equations (1) and (32) constitute the system of equations we must solve. In general it will be necessary to resort to numerical means for this task, but for the case of an unperturbed laminar ionosphere it is both possible and useful to find a simple analytic solution to the plasma flow field, which is an illuminating example.

Suppose Σ_{p1}, Σ_{p2}, Σ_{p3}, are functions only of y (altitude in the equatorial plane). Then for any set of boundary conditions on ϕ which does not itself impose an x-dependence on ϕ, we find that $\phi = \phi(y)$. Then (32) becomes

$$\frac{\partial}{\partial y}\left((\Sigma_{p1} + \Sigma_{p2} + \Sigma_{p3})\ \frac{\partial\phi}{\partial y}\right) = -\frac{\partial}{\partial y}\ \left(\Sigma_{p2}\ \Omega_i\ \frac{m_i}{e}\ U_n\right) \tag{35}$$

the general solution of which is

$$(\Sigma_{p1} + \Sigma_{p2} + \Sigma_{p3}).\ \frac{\partial\phi}{\partial y} = -\Sigma_{p2}\Omega_i\ \frac{m_i}{e}\ U_n + J_{oy} \tag{36}$$

where J_{oy} is a constant, and we have dropped the subscript 2 on Ω_i, m_i, and U_n. Assuming that $\Sigma_{p2} \to 0$ as $y \to \pm\infty$ and demanding that $\frac{\partial\phi}{\partial y}$ (or equivalently

the total current) vanish at $y = \pm \infty$ we get $J_{oy} = 0$. Recalling that $\frac{\partial \phi}{\partial y} = - E_y$ we obtain

$$E_y = \frac{\Sigma_{P2}}{\Sigma_{P1}+\Sigma_{P2}+\Sigma_{P3}} \quad \Omega_i \quad \frac{m_i}{e} \quad U_n \tag{37}$$

The $\underline{E}\times\underline{B}$ plasma motion produced by this electric field is given by

$$v_x = \frac{cE_y}{B} = \frac{\Sigma_{P2}}{\Sigma_{P1}+\Sigma_{P2}+\Sigma_{P3}} \quad \frac{c}{B} \quad \Omega_i \quad \frac{m_i}{e} \quad U_n \tag{38}$$

$$= \frac{\Sigma_{P2}}{\Sigma_{P1}+\Sigma_{P2}+\Sigma_{P3}} \quad U_n$$

$$= f \; U_n$$

where

$$f = \Sigma_{P2} / \; (\Sigma_{P1}+\Sigma_{P2}+\Sigma_{P3}) \tag{39}$$

Note that the plasma drifts at a fraction f of the neutral wind velocity, and that that fraction is simply the ratio of the "local" (i.e., equatorial plane) Pedersen conductivity to the total field line conductivity on a given field line (Note: what we have in mind here and in the numerical simulations is that our magnetic field line integration for the equatorial F region is over a few degrees in latitude, and that regions 1 and 3 constitute the rest of the field line connected ionosphere as a load on the circuit). This simple equation has some remarkable consequences in terms of the motion of structures (spread F plumes, for example) imbedded in the equatorial ionosphere. Suppose that Σ_{P2} is a function of altitude with a peak Σ_{P2}^{max} at altitude h_{max}. Suppose further that Σ_{P1} and Σ_{P3} are constants such that $\Sigma_{P1} + \Sigma_{P3} = 0.1 \; \Sigma_{P2}^{max}$, and that we impose a uniform eastward neutral wind of 100 m/sec on level 2 (the equatorial plane). We now create a model ionosphere (see Table 1) and

tabulate the eastward plasma velocity as a function of altitude:

TABLE 1

Altitude (km)	$\Sigma_{P2}/\Sigma_{P2}^{max}$	Eastward Plasma Velocity (m/sec)
600	0.1	50
500	0.5	83
400 (h_{max})	1.0	91
300	0.1	50
200	0.01	9

Note that even though there is no vertical shear in the neutral wind velocity, the plasma flow field contains a large shear with opposing signs on either side of h_{max}. The effect of this shear is to bend any passive vertical structure imbedded in this flow field into a "C" shape as depicted in Figure 3 (Also note that for $\Sigma_{P1} = \Sigma_{P3} = 0$, i.e., no E region, from (39) $f = 1$ and the plasma moves at the wind speed (Rishbeth, 1971)).

The above result is quite satisfying in that it offers a qualitative explanation of the "C's", "fishtails", and other tilted structures seen by Woodman and La Hoz [1976] and Tsunoda [1981] in their observations of coherent radar backscatter from the meter-scale irregularities associated with ESF plumes. However, the above analysis is valid only for passive structures imbedded in a laminar unperturbed ionosphere, conditions which are simply not met in the ESF environment. Numerical simulations are necessary to prove the case unequivocally.

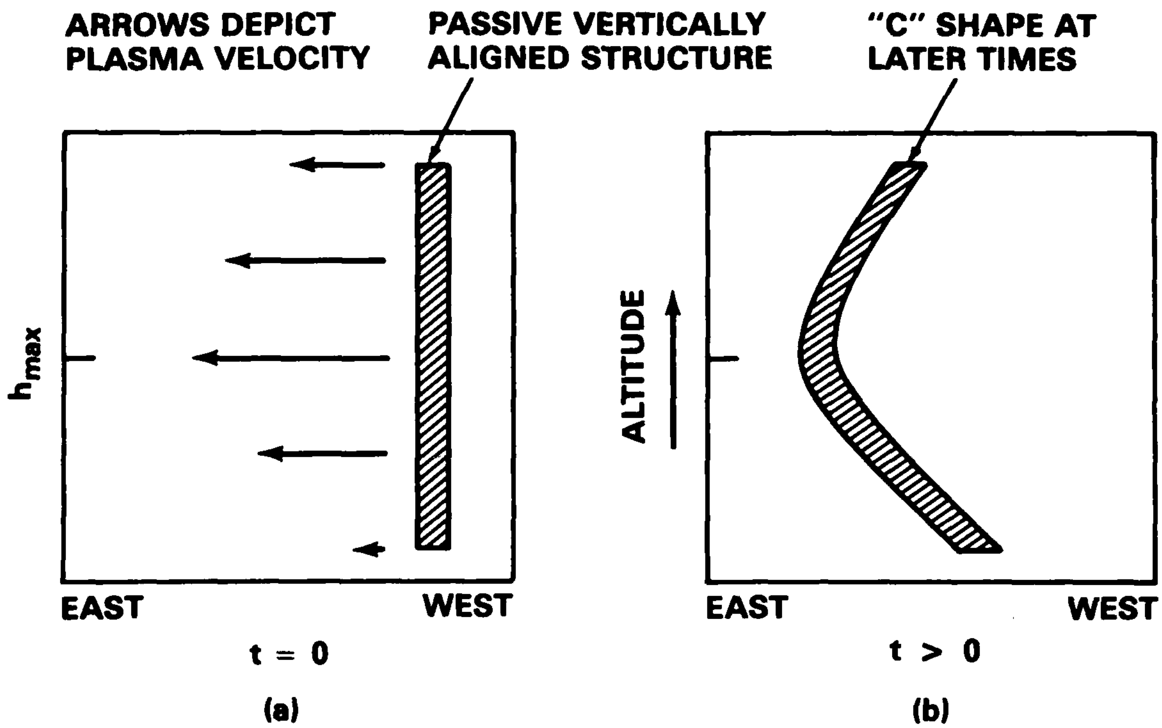

Fig. 3 — Schematic diagram depicting the bending of a passive vertically-aligned structure caught up in a velocity shear pattern of the type we believe exists in the nighttime equatorial ionosphere. The neutral wind is eastward and uniform in altitude, and the response of the plasma (depicted by arrows) is to move at some fraction of the neutral wind velocity, that fraction being largest at the altitude h_{max} of maximum equatorial plane Pedersen conductivity. The eastward plasma velocity falls off both above and below h_{max}, as shown.

3. Numerical Simulations

We mentioned before that equations (1) and (32) constitute the system we wish to solve numerically. Let us now be more specific. Equation (1) is actually six equations (one electron and one ion equation for each of our three layers). By quasi-neutrality (17) we can eliminate three of these and integrate either the ion or electron equation at each level; but since we have made the assumption that $\underline{v}_{i\parallel} = 0$ (currents along field lines are carried by electrons) we can more conveniently solve the two-dimensional ion continuity equation at each layer:

$$\left[\frac{\partial n}{\partial t} + \nabla_{\perp} \cdot (n\, \underline{v}_{i\perp}) = -\, \nu_R n\right]_{k};\ k = 1,2,3 \tag{40}$$

In the simulations we present here we have set ν_R in (40) to zero for simplicity and because at the F region altitudes we shall be dealing with, recombination effects are negligible.

We now make one last simplifying assumption: the background E region plasma (layers 1 and 3) is initially uniform in density and Pedersen conductivity, and remains so during the course of our simulation. This is tantamount to neglecting compressibility (Pedersen mobility) effects in the E region plasma. Thus, we are utilizing layers 1 and 3 as a passive load in an ionospheric circuit, in order to allow for short circuiting effects. A true multilevel numerical code which will model these effects self-consistently is under development. This assumption does have the advantage, though, of reducing (40) to a single equation (since $\partial n/\partial t = 0$ for levels 1 and 3) and of eliminating H and the last two terms of (32) (since all the terms subscripted by b are constant). Our final pair of equations to be solved numerically is then

$$\frac{\partial n}{\partial t} + \nabla_{\perp} \cdot (n\, \underline{v}_{i\perp}) = 0 \tag{41}$$

$$\nabla_{\perp} \cdot \left[(\Sigma_{p1} + \Sigma_{p2} + \Sigma_{p3}) \nabla_{\perp} \phi \right] = - \frac{\partial}{\partial x} \left[\Sigma_p \frac{Bg}{\nu_{in} c} \right] - \frac{\partial}{\partial y} \left[\Sigma_p \frac{BU_n}{c} \right] \tag{42}$$

where all quantities except Σ_{p1} and Σ_{p3} refer to layer 2.

Equation (41) is solved numerically using the fully multi-dimensional flux-corrected transport (FCT) techniques of Zalesak [1979]. Briefly, FCT is a technique originally developed by Boris and Book [1973] for solving equations of the form (41) where steep gradients in n are expected to form. The fluxes used in the algorithm are nonlinear weighted averages of fluxes computed by high and low order finite differences. The high order fluxes are weighted as heavily as possible subject to the constraint that nonphysical oscillations are not introduced. Equation (42) is solved using the fully vectorized incomplete Cholesky conjugate gradient (ICCG) algorithm of Hain [1980], which is an extension of the work of Kershaw [1978]. This algorithm is extremely fast and efficient for the cases described below for which the neutral wind was set to zero; however, when a finite eastward neutral wind was used the ICCG convergence rate became painfully slow and it was necessary to resort to the direct elliptic solver of Madala [1978].

The numerical calculations to be presented were performed on a two-dimensional cartesian mesh using 40 points in the x (east-west) direction and 140 points in the y (vertical direction). The (uniform) grid spacing was 3 km in the y direction, and 5 km is the x direction for all calculations. Note that in our previous work we used 2 km spacing in the y direction. The bottom of the grid corresponds to 253 km altitude and the top of the

grid to 676 km altitude. Periodic boundary conditions were imposed on both n and ϕ in the x direction. In the y direction transmissive boundary conditions were imposed on n ($\partial n/\partial x = 0$), and the normal derivative of ϕ at the top boundary was chosen such that the normal component of the total current (the sum over all three layers) was zero there for the unperturbed state. For the calculations with no neutral wind this implies $\partial\phi/\partial y = 0$ at the upper boundary. For calculations with a neutral wind this implies

$$(\Sigma_{p_1}^{o}+\Sigma_{p_2}^{o}+\Sigma_{p_3}^{o}) \frac{\partial\phi}{\partial y} + \left[\Sigma_p^o \Omega_i \frac{m_i}{e} U_n\right]_2 = 0 \tag{43}$$

at the upper boundary, where Σ_p^o is the Pedersen conductivity of the initial unperturbed state. At the lower boundary we set $\phi = 0$ for all cases.

Three kinds of plots will be presented: (1) contours of constant $n(x,y,t)$; (2) contours of constant $n(x,y,t)/n_o(y)$; and (3) contours of constant electrostatic potential $\phi(x,y,t)$. Here $n_o(y)$ is the initial unperturbed electron density profile in layer 2. Superimposed on each contour plot is a dashed line depicting $n_o(y)$ for reference purposes. Our $n_o(y)$ profile is such that the F_2 peak is located at 434 km altitude, and the minimum electron density scale length $L = n_o(\partial n_o/\partial y)^{-1}$ is 10 km. The ion-neutral collision frequency $\nu_{in}(y)$ used in the calculations is shown in Figure 4. The initial perturbation used to start each calculation was a mode 1 sine wave in the x direction:

$$\frac{n(x,y,0)}{n_o(y)} = 1 - e^{-3} \cos (\pi x/100) \tag{44}$$

Three calculations were performed to determine the effect of the

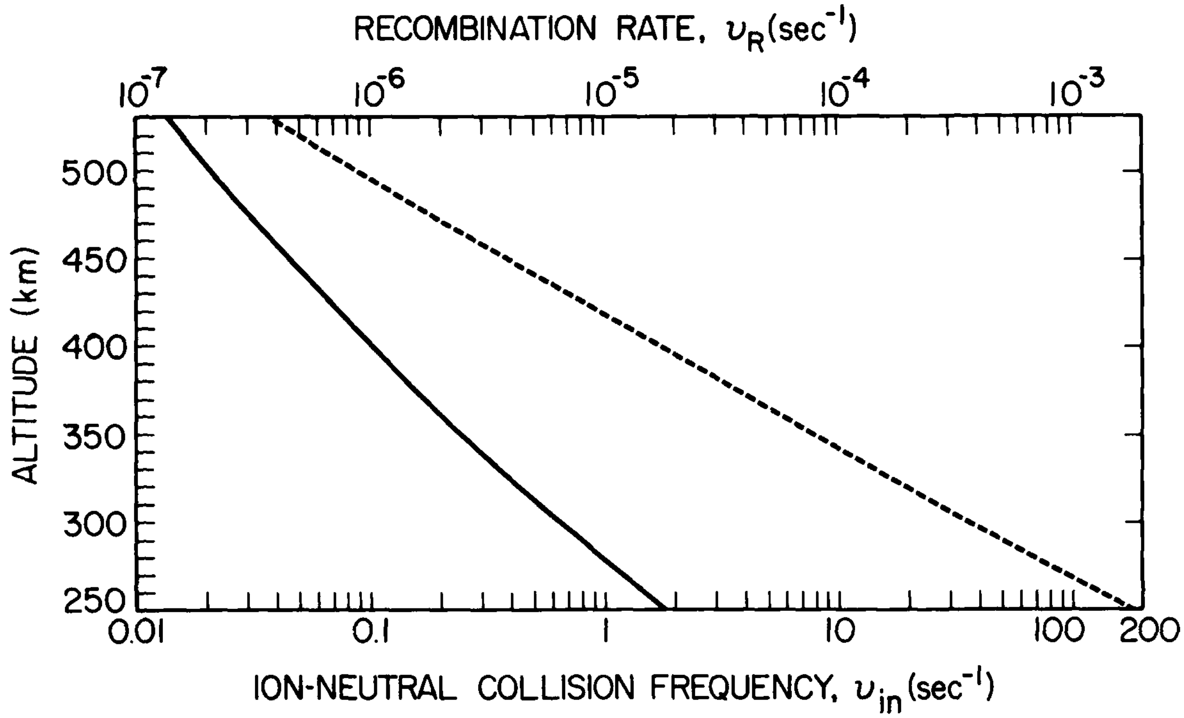

Fig. 4 — The ion-neutral collision frequency ν_{in} (solid line) as a function of altitude. The recombination coefficient ν_R was set to zero for this study (see text).

background E region plasma and of the eastward neutral wind on evolving spread F bubbles:

1) Calculation 2L, in which $\Sigma_{p_1} = \Sigma_{p_3} = U_n = 0$. This calculation is identical to calculation 2L of Zalesak and Ossakow [1980] except for the difference in vertical grid spacing noted previously.

2) Calculation 2LE, identical to calculation 2L above, except that a constant background Pedersen conductivity has been included such that $\Sigma_{p_1} + \Sigma_{p_3} = 0.12\ \Sigma^o_{2max}$, where Σ^o_{2max} is the maximum Pedersen conductivity in the initial unperturbed equatorial plane (layer 2). We believe the value of 0.12 for the relative background Pedersen conductivity level to be a conservative figure. Rishbeth [1971] used a value of 0.2 as being representative of nighttime conditions.

3) Calculation 2LEW, identical to calculation 2LE above, except that a uniform eastward neutral wind of 150 m/sec was imposed over the entire equatorial plane (U_n = - 150 m/sec). The designations E and W above obviously refer to the presence of E region plasma and neutral winds, respectively.

Figure 5 shows isodensity contours of n(x,y,0) for our initial conditions (laminar ionosphere $n_o(y)$ plus perturbation (44)). The contours are labeled for later reference purposes. Note that in this and all subsequent plots we have plotted two periods (recall that we have periodic boundary conditions in the x direction) of the various functions. That is, the 40 by 140 mesh was extended to 80 by 140 for plotting purposes only, to facilitate comparison with plots of calculations run with a neutral wind, in which structures move across the grid.

Figure 6 shows isodensity contours of n(x,y,t) for calculation 2L at four different times during the simulation. Figure 7 shows a similar sequence

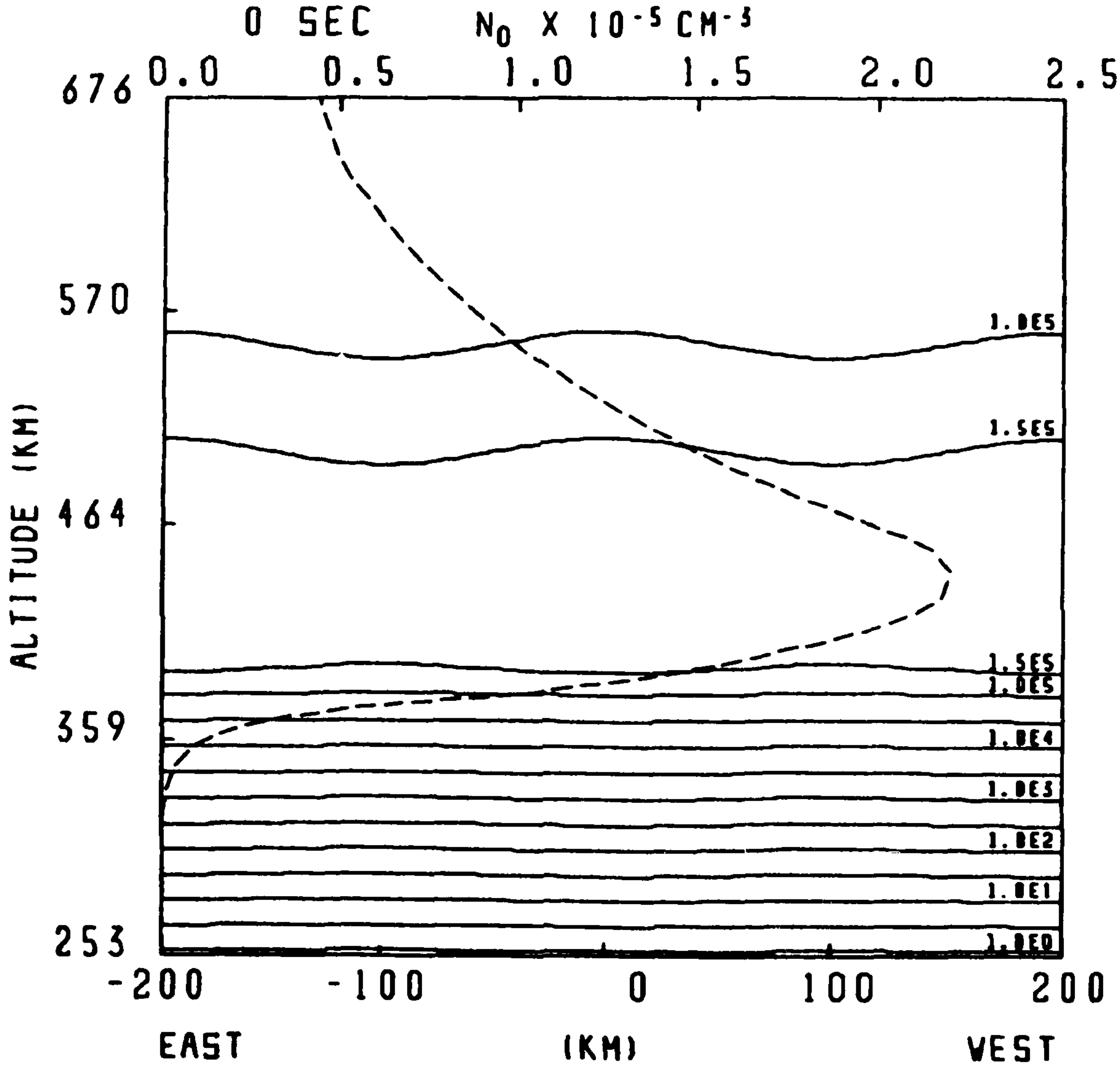

Fig. 5 — Iso-electron density contours for the initial perturbed state in layer 2. This represents the initial conditions for our numerical simulation. The contours are labeled in units of electrons/cm^3 in E format notation (1.0E1 = 1 × 10^1, etc.). The unperturbed ionosphere was initially laminar (independent of x, the east-west direction) and is exhibited by the dashed curve showing $N_o(y)$, at any point in the east-west (x) direction. This curve is labeled at the top of the figure. The perturbation has a maximum amplitude of e^{-3} in relative electron density, is a pure mode 1 sine wave in x, and is independent of altitude y, as described in the text. The observer is looking southward so that $\underline{B}$ is out of the figure.

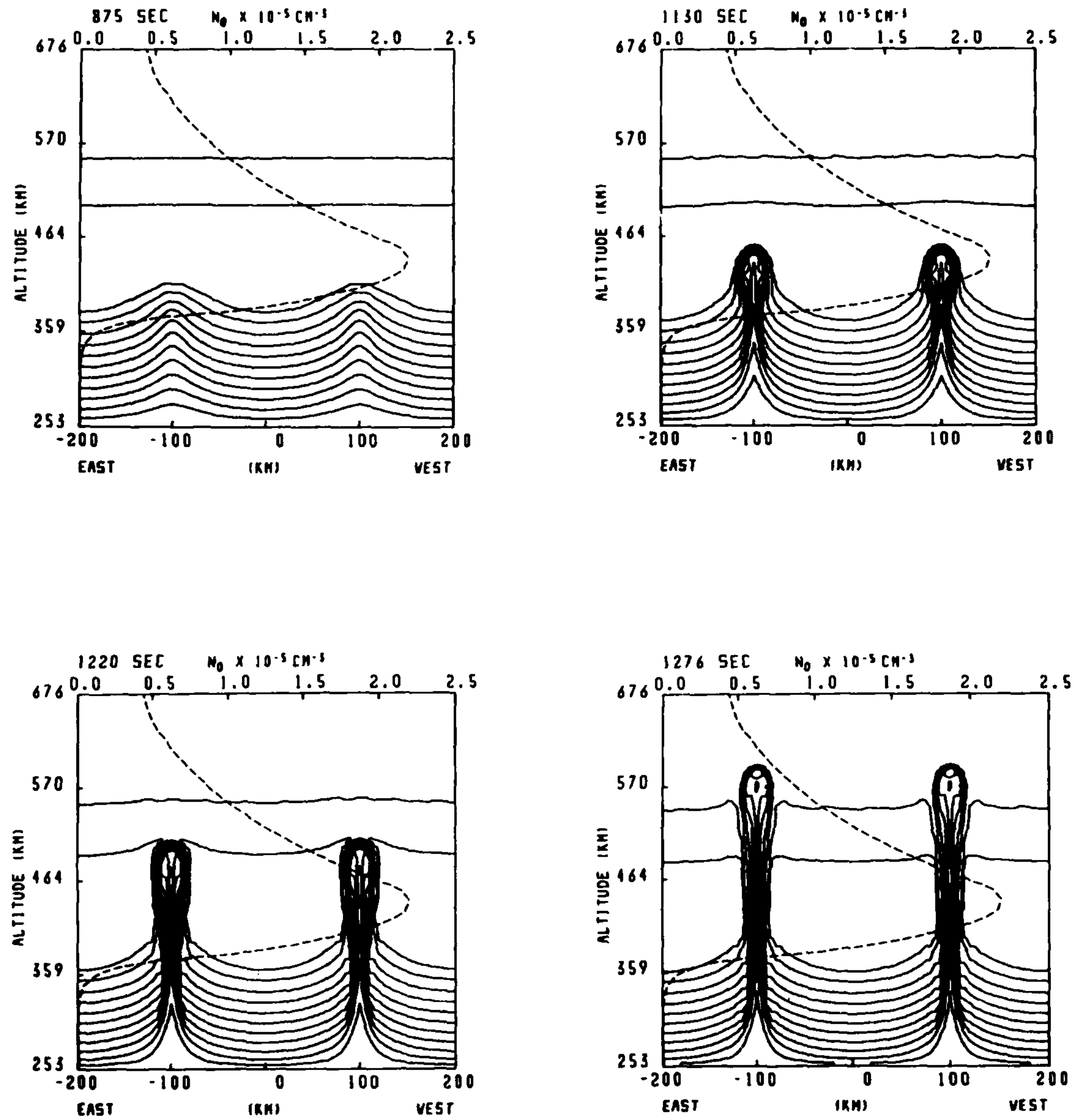

Fig. 6 — Sequence of four iso-electron density contours for calculation 2L (no backbround, no wind) at 875, 1130, 1220, and 1276 seconds

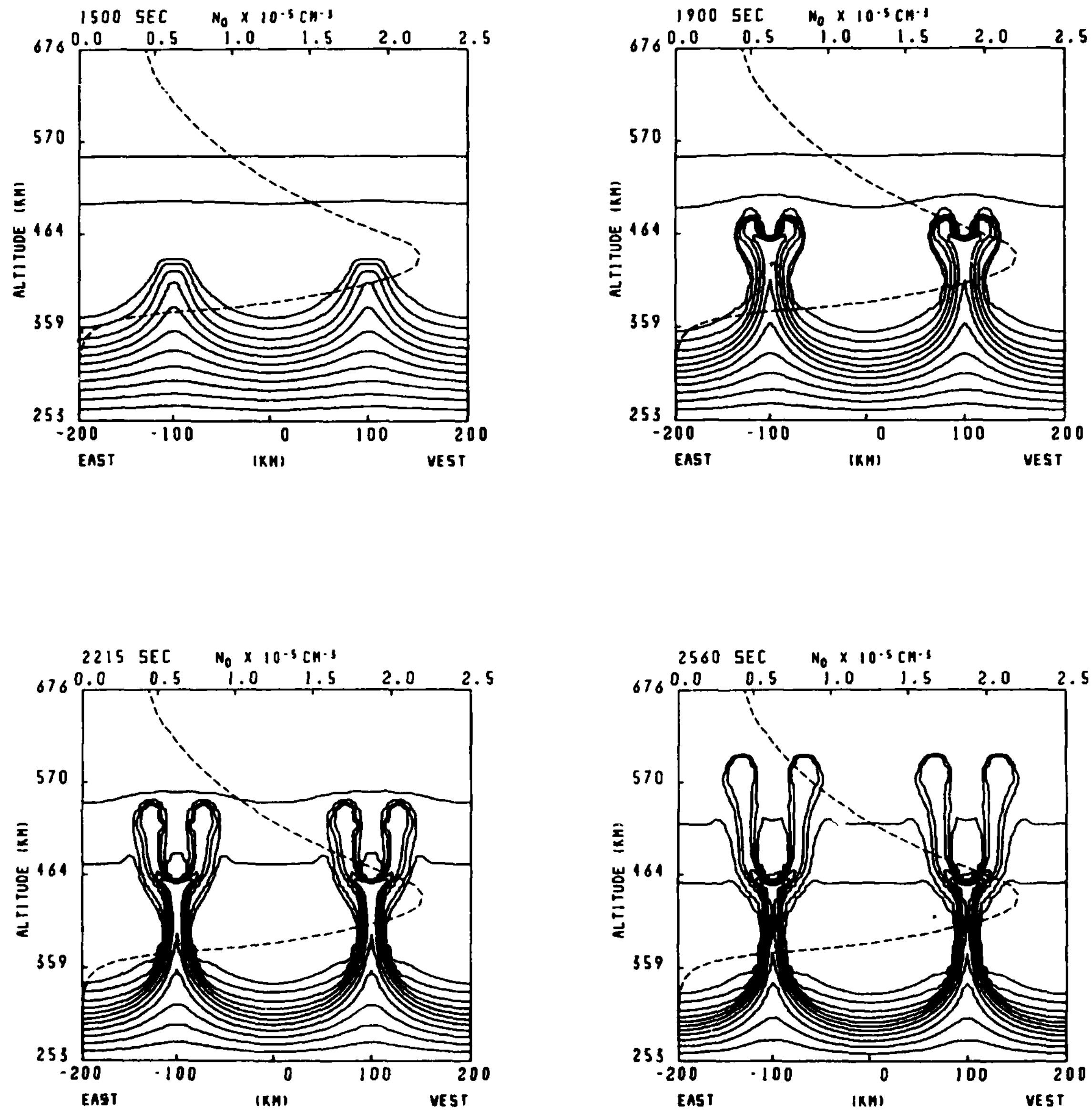

Fig. 7 — Same as Figure 6, but for calculation 2LE (background E region, no wind) at 1500, 1900, 2215, and 2560 seconds

for calculation 2LE. (The reader may note that the 2L calculation of this paper evolves at a faster rate at late times than the 2L calculation of Zalesak and Ossakow [1980]. This is primarily due to two improvements in the numerical treatment of equations (41) and (42), implemented since our previous studies: 1) the differencing of the Hermitian form (42) of the potential equation, rather than the non-Hermitian expansion we were constrained to use previously, as discussed in the appendix of Zalesak and Ossakow [1980]; and 2) improved treatment of the continuity equation (41) which has enabled us to further reduce the numerical diffusion that inevitably occurs across electron density gradients as steep as those formed at the edges of ESF plumes at late times. We would emphasize that the conclusions of Zalesak and Ossakow [1980] do not depend on late-time rise velocities and are, therefore, unaffected by this result). In comparing Figure 6 with Figure 7 we are looking at the effect of a background conductivity. The most striking difference is that of the time scales, whereby 2LE takes about 70% more time to achieve a 600 km altitude plume than does 2L. Qualitatively this can be understood in terms of the shorting effect of the background E region, by which a given current can be driven by a smaller electric field, which in turn means smaller plasma velocities. Almost as striking is the fact that the 2LE plume bifurcated while the 2L plume did not. The inevitability of the bifurcation in calculation 2LE can be seen even in the very early time plot at 1500 sec, where the characteristic flattening of a significant number of contours in the upper portion of the plume, the sure signal of imminent bifurcation in barium cloud studies [Zabusky et al., 1973; Scannapieco et al., 1974; Ossakow et al., 1977; McDonald et al., 1980], can be seen. The close similarity of the physics of the ESF gravitational instability and that of the ExB gradient drift instability associated with the bifurcation and striation process in plasma

clouds, has been noted by Scannapieco and Ossakow [1976]. We shall draw heavily on our knowledge of bifurcation tendencies in plasma clouds [Ossakow et al., 1977; McDonald et al., 1980] when we address the question of why the plume in calculation 2LE bifurcated while that in calculation 2L did not, later in this paper.

For the moment we note that there are two primary effects of the presence of a background conducting region (E region): 1) electric fields everywhere are reduced by the shorting effects of the background conductivity, resulting in an overall slower evolution for the instability; and 2) electric fields are reduced the most in the regions where the ratio of the equatorial plane conductivity to that of the background plane is smallest, i.e., at low altitudes, rendering the 2LE configuration incapable of drawing plasma from extremely low altitudes to produce large depletion levels inside the bubble. This can be seen easily in comparing Figures 6 and 7 wherein we note that the isodensity contours at low altitudes are virtually stationary in the 2LE case, whereas the 2L configuration results in significant upward movement in even the lowest density plasma near the bottom of the plot. The more effective shorting of the electric fields by the background layer in the 2LE case is seen dramatically in Fig. 9a and 9b, where we plot contours of constant electrostatic potential ϕ for calculations 2L and 2LE respectively at early time. (The contour level increment of ϕ in this paper is chosen such as to divide the maximum excursion of ϕ from zero into 7 equal intervals. The contours corresponding to positive values of ϕ are plotted as solid lines, while those corresponding to negative values are plotted as dashed lines. The zero contour level is suppressed. For the 2L and 2LE cases the symmetry of the potential would cause the zero contour to be simply two vertical lines. Since the electric field, and hence plasma velocity, is

inversely proportional to the contour spacing, this normalization allows us to easily determine by eye the rate at which the upward velocity of plasma is decreasing with decreasing altitude. It also allows us to visualize the global plasma flow field, since contours of ϕ are essentially streamlines of the plasma flow). Comparing Figures 9a and 9b, we note a much more rapid decrease in the horizontal component of the electric field with decreasing altitude in calculation 2LE than in 2L. The flow field in 2LE is mixing plasma over a fairly narrow altitude range, while that in 2L is drawing plasma from deep in the ionosphere, where the plasma densities are lowest. Hence, we should expect the late time plume in calculation 2L to consist of plasma of lower density (i.e., to have much higher depletion levels) than that in calculation 2LE. That this is indeed the case can be seen in Figures 10a and 10b, where we compare isodensity contours of $n(x,y)/n_o(y)$ at late times for the two calculations. (Contours of n/n_o in this paper are spaced logarithmically, with solid lines representing depletions ($n/n_o<1$) and dashed lines representing enhancements ($n/n_o>1$). The kth depletion contour represents an n/n_o value of 0.5^k, while the kth enhancement contour represents an n/n_o value of 2.0^k). Although the bifurcation of the 2LE plume makes the comparison less clean than it would otherwise be, it is obvious that the depletion levels of the 2L plume are much higher than those of the 2LE plume. Depletion levels ($1-n/n_o$) in the upper portions of the 2L plume are greater than 99.2%, while those in the 2LE plume are only about 94%. We conclude that the presence of a background conducting region results in plumes which are both slower to evolve and less depleted than their no-background conterparts.

In Figure 8 we present isodensity contours of calculation 2LEW at times similar to those presented for the 2LE calculation. For the $\nu_{in}(y)$ and $n_o(y)$ profiles chosen we find a peak in Σ^o_{P2} at 394 km, 40 km below the F2 peak, with

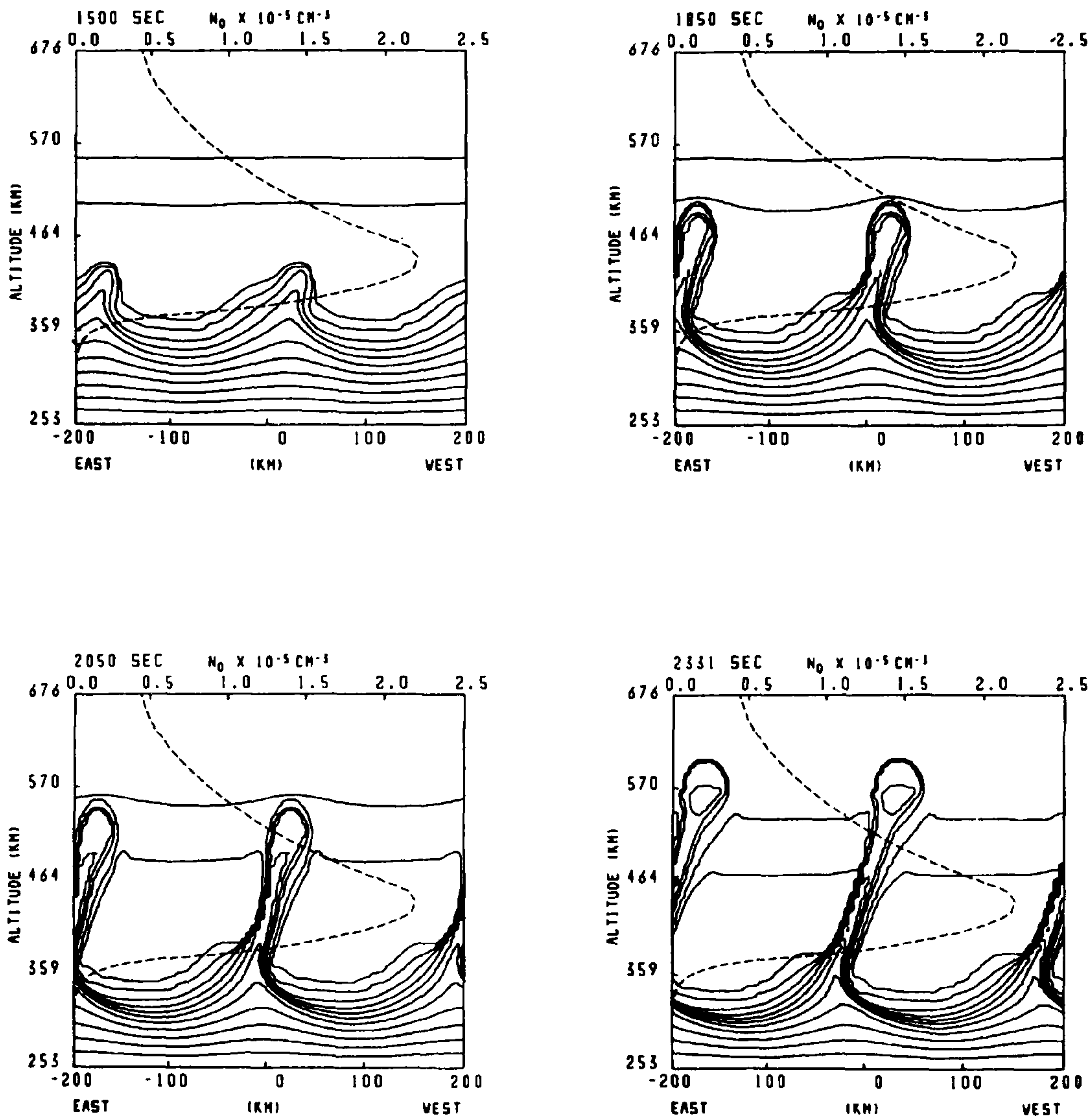

Fig. 8 — Same as Figure 6, but for calculation 2LEW (background plus wind) at 1500, 1850, 2050, and 2331 seconds. Our reference frame is moving eastward at 68 m/sec.

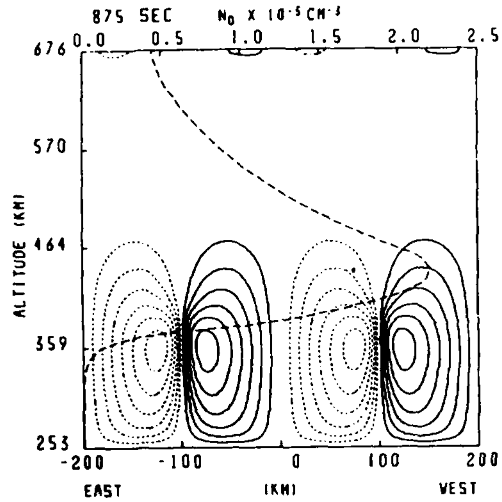

(a)

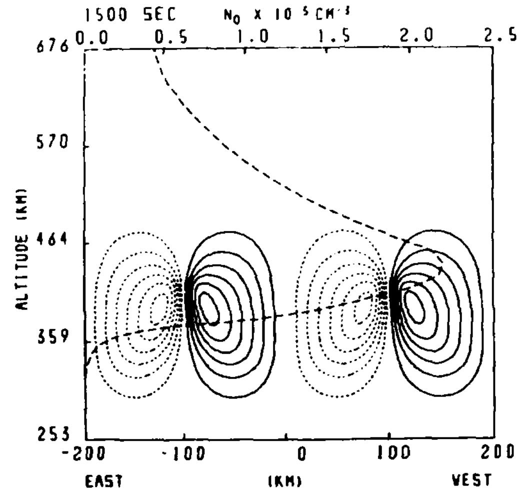

(b)

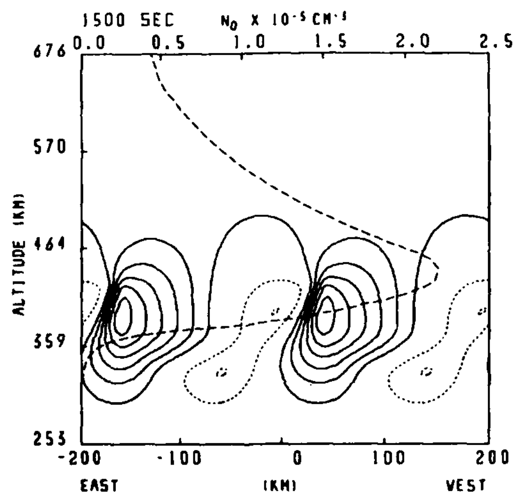

(c)

Fig. 9 — Early time contours of constant electrostatic potential $\phi(x,y)$ for (a) calculation 2L at 875 sec, (b) calculation 2 LE at 1500 sec and (c) calculation 2 LEW at 1500 sec. The potential $\phi_o(y)$ associated with the unperturbed initial conditions has been removed in (c). The contour level increment is chosen such as to divide the maximum excursion of ϕ from zero into 7 equal intervals. The contours corresponding to positive values of ϕ are plotted as solid lines, while those corresponding to negative values are plotted as dashed lines. The zero contour level is suppressed.

Σ^{o}_{p2} falling off by a factor of ten 42 km below and 132 km above this altitude (at 352 km and 526 km altitude respectively). Using Equation (38) to approximate our initial shear field and using $\Sigma_{p1} + \Sigma_{p3} = .12\ \Sigma^{max}_{2}$ we find eastward plasma drifts of 134 m/sec at 394 km altitude and 68 m/sec at both 352 and 526 km altitude. The plasma shear is weaker, but over a larger altitude range, above the peak in Σ_2 than below it. If vertical plasma plumes behave as passive structures, we would expect a bending of the structure around an altitude of 394 km, with a larger slope below this altitude than above it. Looking at Figure 8 we see that this behavior is qualitatively reproduced, in spite of the fact that the self-consistent polarization fields produced by the plumes represent very large perturbations on the equilibrium fields producing the plasma shear. In Figure 8 we have placed ourselves in a frame moving at 68 m/sec eastward to minimize both computational errors and computer time. In Figure 10c we show late time isodensity contours of $n(x,y)/n_o(y)$ for calculation 2LEW, for comparision to Figures 10a and 10b. The bending of the plume into a "C" shape about an altitude of 360 km is quite pronounced. The fact that this "bending point" is more than 30 km below the initial maximum in equatorial plane Pedersen conductivity is an indication of a nonlinear interaction between plume rise and ambient plasma shear. In fact, this shift downward can be understood qualitatively as follows. The movement of low density plasma upward inside the plume is accompanied by the movement of high density plasma downward in the regions between the plumes (see Figures 9 and 10). Since the scale length over which ν_{in} is decreasing with altitude is long ($\sim$60 km) compared to the scale length over which the electron density is increasing with altitude ($\sim$10 km) below the F2 peak, the effect of this downward movement of high density plasma is to move the point of maximum Pedersen conductivity in the equatorial plane and hence the bending

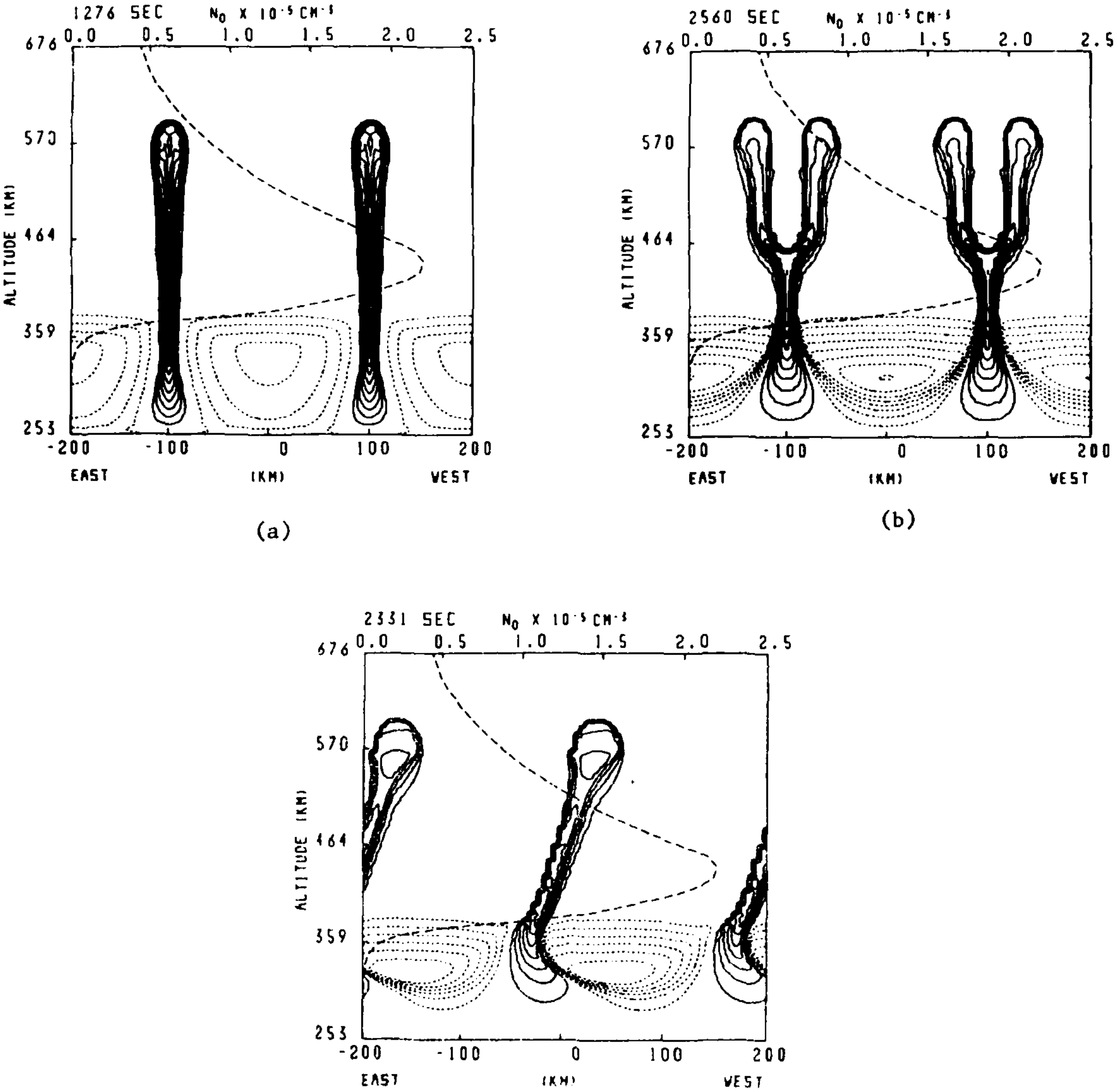

(a)

(b)

(c)

Fig. 10 — Late time contours of constant $n(x,y)/n_o(y)$ for (a) calculation 2L at 1276 sec, (b) calculation 2LE at 2560 sec, and (c) calculation 2LE at 2331 sec. The contours are spaced logarithmically, with solid lines representing depletions ($n/n_o<1$) and dashed lines representing enhancements ($n/n_o>1$). The k<u>th</u> depletion contour represents an n/n_o value of 0.5^k, while the k<u>th</u> enhancement contour represents an n/n_o value of 2.0^k.

point, downward.

In Figure 9 c, we show contours of constant $\phi(x,y)-\phi_o(y)$ at 1500 sec for calculation 2LEW, for comparison to Figures 9a and 9b. Here $\phi_o(y)$ is the initial equilibrium electrostatic potential of the unperturbed initial conditions (for the 2L and 2LE cases $\phi_o = 0$). Subtracting this quantity from ϕ before plotting enables us to examine the "underlying" plume motion on which the shear associated with the initial conditions is superposed. Remarkably, the motion of plasma in the plume is not purely upward, but rather upward and <u>westward</u>, despite the fact that we have removed the asymmetry-inducing profile of the equilibrium initial wind field. Although this simple analysis is crude (in that the dependence of ϕ on the plasma structure is not linear, i.e., in Eq. (42) if $\phi^A(x,y)$ and $\phi^B(x,y)$ are solutions for $\Sigma^A_{P2}(x,y)$ and $\Sigma^B_{P2}(x,y)$ respectively, $\phi^A(x,y) + \phi^B(x,y)$ is not a solution for $\Sigma^A_{P2}(x,y) + \Sigma^B_{P2}(x,y)$), it would seem to lend support to the ideas advanced by Woodman and La Hoz [1976], Ossakow and Chaturvedi [1978], and Ott [1978] who proposed that a neutral wind whose eastward velocity exceeded that of the plasma would combine with gravity to form an effective gravity which pointed downward and eastward, causing bubbles or plumes to drift upward and westward relative to the surrounding plasma. Thus, the westward tilt of plumes at high altitudes would appear to be due to both this effect (since we have shown that the plasma velocity <u>does</u> lag the neutral wind velocity) <u>and</u> that of the plasma shear which we have addressed earlier. We would point out, however, that the mechanism of Woodman and La Hoz [1976], Ossakow and Chaturvedi [1978], and Ott [1978] cannot explain the eastward tilt of plumes with altitude at low altitudes.

In comparing calculations 2LE and 2LEW (Figures 7 and 8), we are

evaluating the effect of the neutral wind itself, since the same background Pedersen conductivity was used in both cases. We wish to note the following points: 1) the two calculations evolve at approximately the same rate in time; 2) the primary effect of the wind is to bend the plume in calculation 2LEW into a "C" shape, with the upper part of the "C" being much larger in altitude extent and tilted markedly westward; 3) the plume depletion levels are approximately the same in both calculations; and 4) the 2LE plume bifurcated while the 2LEW plume did not. We shall address this last question, along with the question of why the plume in calculation 2L did not bifurcate in the next section.

4. Discussion and Conclusions

Before proceeding with further discussion of our numerical results, let us try to lend support to the idea that these tilted and C-shaped plumes are, in fact, seen in equatorial spread F. We present experimental radar backscatter maps of meter scale plasma irregularities taken during equatorial spread F. Figure 11 shows a map of 3 meter irregularities (provided by J.P. McClure) using the Jicamarca radar. Similar plots can be found in Woodman and La Hoz [1976]. Figure 12 shows a map of 1 meter irregularities taken by Tsunoda [1981] using the ALTAIR radar. We refer the reader to the respective papers for a detailed explanation of these plots, but we point out that the Jicamarca radar scans a fixed line in space, and plots backscatter strength as a function of time. Therefore, structures caught up in our postulated plasma shear would have their C-shaped appearance exaggerated in the Jicamarca plots. The ALTAIR radar, however, is steerable; and it's backscatter plots are a good approximation to a "snapshot" of the backscatter strength at a single time. In both plots the evidence of oppositely tilting structures at high and low altitudes is apparent. In making comparisons with these small scale ($\leq$ 3m) irregularity radar backscatter maps we are assuming that these maps are signatures (Tsunoda, 1980) of the large scale size bubbles depicted in Figure 8. That is the steep plasma density gradients associated with the bubbles in Figure 8 drive the radar backscatter observed irregularities. The westward and upward motion of the bubbles depicted in Figure 8 is in agreement with the satellite in situ measurements of McClure et al., [1977].

It is our belief that the arguments advanced in this paper offer the most plausible explanation yet of the qualitative behavior of equatorial

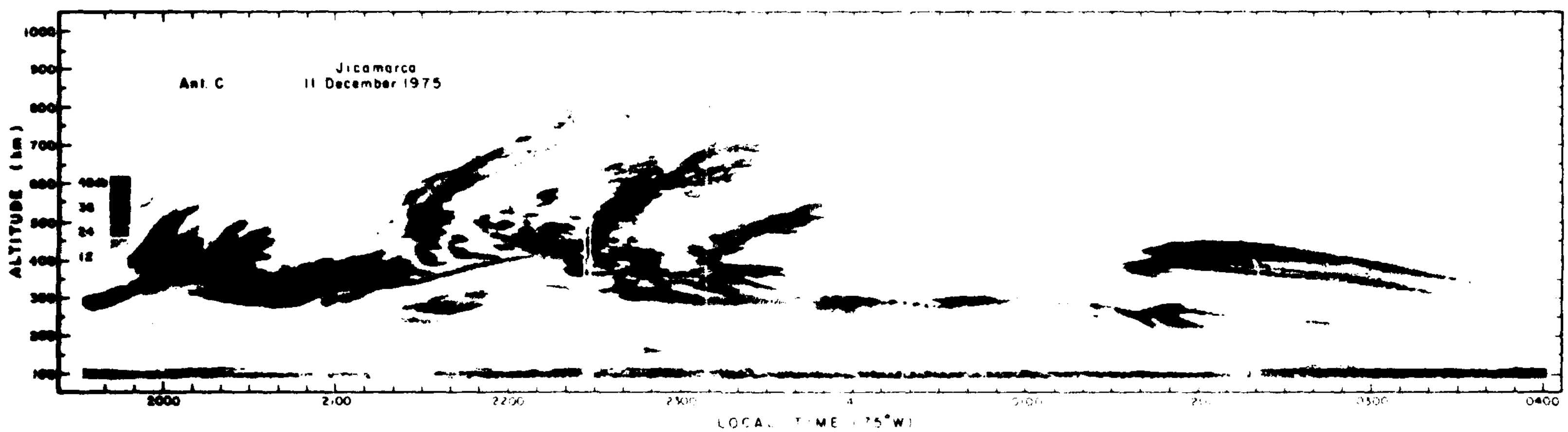

Fig. 11 — Map of 3 meter irregularities taken by the ground based Jicamarca radar, during equatorial spread F, supplied by J.P. McClure. The stationary radar is pointed upward, while irregularities moving eastward sweep past its field of view. Note that the features ("C's" and "fishtails") seen on this altitude vs. time plot are consistent with westward tilts with altitude at high altitudes and eastward tilts with altitude at low altitudes.

Fig. 11

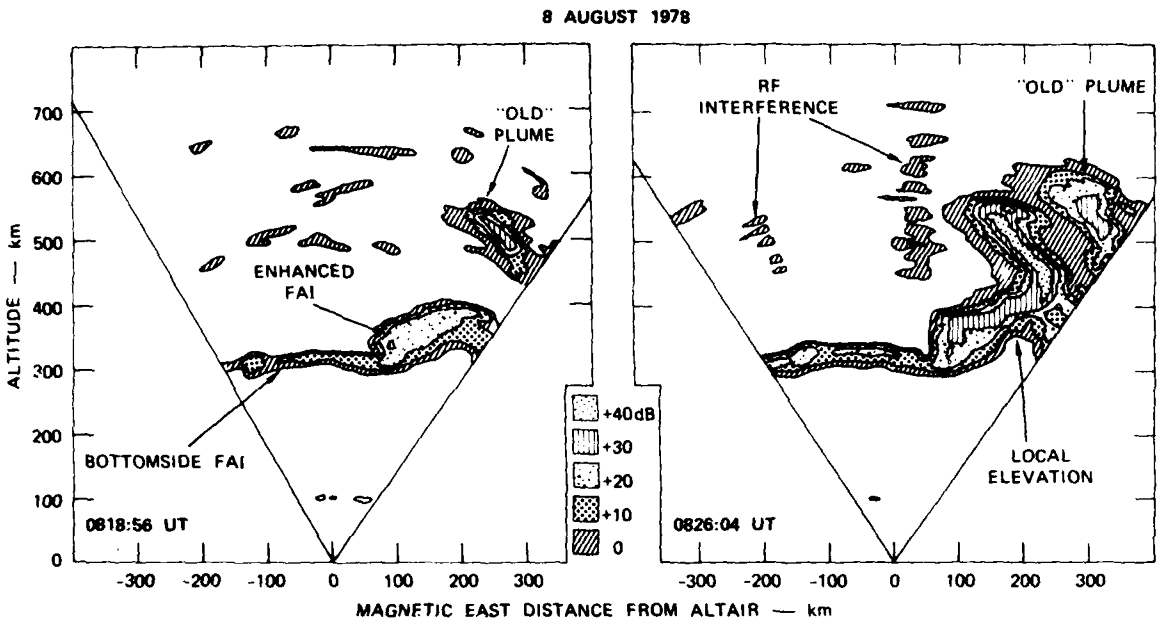

Fig. 12 — Maps of 1 meter irregularities taken by the steerable ALTAIR radar during equatorial spread F, from Tsunoda [1981]. These maps are very close to being snapshots of the locus of irregularities at a given time. Note the oppositely tilting structures at different altitudes in the left-hand map, and the clear bending of a plume into a "C" shape about an altitude of about 400 km in the right-hand plot.

spread F plumes: "C"-shaped structures and westward plume tilts are simply the result of vertically rising spread F plumes being caught up in the ambient plasma shear both as they rise and subsequently, this shear being the natural consequence of a neutral wind at the equator and E regions of finite conductivity connected to the equatorial F region along magnetic field lines. If there is a neutral wind, but no E region, the plasma will move at the wind speed, ESF bubbles will rise vertically, and the attendant radar backscatter maps will show non-tilted (i.e., vertical) plumes, as exhibited in the measurements of Kelley et al., (1981). Furthermore, even without the equatorial F region neutral wind the numerical simulations show that E region Pedersen conductivity can have a dramatic effect on ESF. For example, the results of section 3 show that ESF has been slowed down as has the attendant bubble evolution. In addition, the ESF bubble in the presence of an E region is less depleted than without the E region. This is due to the fact that the E region has a dramatic effect on the induced polarization electric field (see Fig. 9) which causes the rise of the bubble, the fringe field component of which (Zalesak and Ossakow, 1980) determines the region below the F peak from which plasma is drawn (i.e., which plasma makes up the bubble). The presence or absence of an E region could also explain why bubbles (with large depletions) stop rising at altitudes of 400-500 km (see McClure et al., 1977) on some occasions, but not on others. Indeed, in addition to the height of the F peak and bottomside background electron density gradient scale lengths (Ossakow et al., 1979) influencing ESF evolution, the E region conductivity could also determine why one does or does not observe ESF even when the previously mentioned conditions are satisfied. Thus, the E region (even at night) could be a controlling factor in the formation of ESF irregularities

and could account for such things as the longitudinal influence (Basu and Kelley, 1977; Livingston, 1980) on ESF formation and phenomena.

There are two matters, however, which bear further discussion: 1) the question of why the plume in calculation 2LE bifurcated while those in calculations 2L and 2LEW did not; and (2) the question of where along the edge of the primary plumes in calculation 2LEW one should expect to see secondary instabilities. If we note that an equatorial spread F plume (bubble) is nothing more than an inverse plasma cloud "finger" (i.e., an elongated region of low density plasma (an ESF "plume") penetrating a region of high density plasma is the inverse of an elongated region of high density plasma (a plasma cloud "finger") penetrating a region of low density plasma), we find that the question of why the 2LE plume bifurcated and the 2L plume did not has already been answered for us. McDonald et al., [1981] have shown in their study of bifurcation tendencies of plasma cloud fingers that the critical quantity determining the speed with which a plasma finger will bifurcate is M, the ratio of the Pedersen conductivities inside and outside the finger. When M is moderate, in the range 2 to 10, the bifurcation tendency is high, while for M near 1 or M greater than 100, the bifurcation tendency is extremely small. Looking at the 2LE plume (Fig. 7), and recalling that we have a background Pedersen conductivity of 0.12 times the maximum equatorial plane Pedersen conductivity we find that M^{-1} (the relevant quantity since we are dealing with inverse plasma clouds here) in the 2LE plume is about 9, making it a prime candidate for bifurcation; while M^{-1} for the 2L plume (Fig. 6) is about 10^4, indicating a bifurcation tendency near zero. The question of why the 2LEW plume did not bifurcate is a little harder to answer. Based on the arguments advanced above, the 2LEW plume would have

been just as likely a candidate for bifurcation as the 2LE plume. However, we note that the 2LEW plume is rising into a region of very strong plasma shear. Perkins and Doles [1975] have shown that such a shear would provide a stabilizing mechanism for any secondary instability (i.e., bifurcation) which attempted to grow on the topside of the 2LEW plume, although the geometry used in their study was considerably simpler than that associated with a rising ESF plume. We advance this mechanism as a plausible, but less than totally convincing, explanation of why the 2LEW plume did not bifurcate, only because we can provide no other at this time.

The question of secondary instabilities on the perimeters or in the interiors of the plumes is in many ways the most interesting aspect of this study. We will confine ourselves to the 2LEW plume (Fig. 8) at late time (2331 sec) since it is both the most interesting and the most realistic. Given the limited spatial resolution of these numerical studies, it must be realized that the actual numerical simulation of the evolution of small-scale secondary instabilities, within the context of the present simulations, is an impossibility. However, we do have the resolution to be able to observe the precursor of the plasma fluid instabilities that we believe are active: the steepening of electron density gradients. By observing the location of these regions of steepening, and by augmenting this procedure with a cell by cell local stability analysis, we should be able to predict both the location of secondary instabilities and the mechanism causing them. We use the term "local stability analysis" to mean a local evaluation, numerical in this case, of the generalized gradient drift growth rate γ_{GD} given by

$$\gamma_{GD} = \left[\frac{c \, \underline{E} \times \underline{B}}{B^2} - \underline{U}_n - \frac{\underline{g}}{\nu_{in}} \right] \cdot \frac{\underline{\nabla} \Sigma_{P2}}{\Sigma_{P1} + \Sigma_{P2} + \Sigma_{P3}} \tag{45}$$

Note that $\underline{E}$ in Eq. (45) above includes the self-consistant polarization electric field given by the solution to the potential equation (42). The influence of this term on γ_{GD} is large, and any stability analysis which were to ignore these polarization fields would rest on shaky ground. Among the assumptions implicit in the application of Eq. (45) are: 1) the growth rates γ_{GD} are large compared to the speed with which the primary Rayleigh-Taylor mode is evolving; and 2) the $\underline{k}$-vector associated with the growing perturbation is perpendicular to $\underline{\nabla}\Sigma_{p_2}$ (which gives maximum growth).

Looking at Figure 8 at the latest time (2331 sec) we see that the primary regions of steepening are two: the west wall of the plume at low altitudes (below 370 km for this particular model) and the east wall of the plume at higher altitudes (above 370 km). Local stability analysis verifies that these are precisely the regions of largest growth rate for the gradient-drift/gravitational Rayleigh-Taylor instability. A less complete analysis of just the effect of an eastward neutral wind on a more or less vertical plume would predict that only the west wall of the plume would be unstable, but this analysis neglects the effects of the bending of the plume which orients the normally stable east wall of the plume so that it is once again unstable to the gravitational instability, and the effects of the polarization electric field produced self-consistently by the ionosphere-plume system, whose effect is to mitigate the expected wind-driven instability over most of the plume structure. We conclude, then, that for this particular plume, we would expect secondary instabilities along the west wall at low altitudes and along the east wall at high altitudes, with the "switch" taking place at about 370 km altitude. If these instabilities eventually cascade down to smaller and smaller scale sizes (or provide the steep plasma density gradients

necessary for further instability mechanisms), eventually reaching the 1-3 meter scale sizes seen on backscatter radar maps, we would expect the radar maps to trace out the locus of the west wall of the plume at low altitudes, and the east wall at high altitudes, giving rise to an even more exaggerated "C" shape than that of the simulation plume (bubble) itself (see the exaggerated "C" traced out by the locus of steepened gradients in Figure 8 at 2331 sec).

We wish to close this section by briefly reviewing work by other researchers which we believe has relevance to the results presented here. Two recent papers have shown experimental evidence of a shear in east-west plasma motion in the equatorial ionosphere: Kudeki et al., [1981] and Tsunoda et al., [1981]. Both papers show evidence of an increase in eastward plasma velocity with altitude, in agreement with the behavior we postulate here for altitudes below the peak in equatorial F region integrated Pedersen conductivity. It is our belief that experimental observations at even higher altitudes than that examined in the above papers would show a decrease in eastward plasma velocity with altitude at these higher altitudes (and possibly even westward velocities), in a manner similar to that shown in Figure 3. Both Kudeki et al., [1981] and Tsunoda et al., [1981] show evidence of a plasma velocity reversal point, that is, an altitude below the F2 peak below which the plasma velocity actually becomes westward (as the eastward velocity passes through zero). The simple model we have presented here offers no explanation for this phenomenon. The reason is that we have assumed here that the E regions connected to the equatorial F region along field lines are passive and free of any dynamics of their own. Actually, however, these E regions are subject to strong diurnal tidal neutral winds,

which are westward at the times associated with spread F. At equatorial altitudes well below the F2 peak, the field-line integrated Pedersen conductivity is dominated by that of the E regions, and hence the westward neutral winds in the E regions are able to set up polarization electric fields which impress themselves on the equatorial region, causing a corresponding westward drift of plasma in the equatorial plane at low altitudes.

In fact, had we retained the neutral wind terms in layers 1 and 3, Eq. (38) would have become

$$V_x = (\Sigma_{p_1} U_{n_1} + \Sigma_{p_2} U_{n_2} + \Sigma_{p_3} U_{n_3})/(\Sigma_{p_1} + \Sigma_{p_2} + \Sigma_{p_3}) \tag{46}$$

where U_{n_1}, U_{n_2}, and U_{n_3} are the east-west neutral winds in layers 1, 2, and 3 respectively. If U_{n_2} is eastward and both U_{n_1} and U_{n_3} are westward, it is obvious that westward plasma velocities will exist at any altitude for which

$$\Sigma_{p_2} < \left| \frac{\Sigma_{p_3} U_{n_3} + \Sigma_{p_1} U_{n1}}{U_{n_2}} \right| \tag{47}$$

This effect and the consequent plasma velocity reversal point were first described by Hellis et al., [1974], whose detailed self-consistent numerical model of the E-and F-region neutral gas and plasma system also shows both the plasma shear and an altitude at which the eastward plasma velocity maximizes, as we have proposed here. In fact, at extreme equatorial F region altitudes, plasma well away from the equatorial plane (both E and F region plasma) may again dominate the integrated Pedersen conductivity, and if the corresponding neutral winds are westward, we should expect to see

westward plasma drifts at these high altitudes, as mentioned above.

The influence of contributions to field line integrated conductivity from plasma away from the equatorial plane on the rise of ESF bubbles has also been addressed by Anderson and Haerendel [1979]. In their model they incorporated flux tube integrated quantities of electron content and Pedersen conductivity and utilized a one-dimensional sheet model for the bubble. This latter assumption resulted in a simple algebraic expression for the induced polarization electric field inside the bubble in terms of the flux tube integrated quantities. ESF bubble rise in the collision dominated Rayleigh-Taylor regime with and without an ambient eastward electric field, $\underline{E}_o$, was investigated. These authors noted that flux tube integrated quantities could have a considerable influence on the outcome of ESF bubble rise, an observation consistent with our comparison of the 2L and 2LE cases. Burke [1979] analyzed the effect of the sunrise "turning-on" of the E region and its subsequent contribution to the demise of ESF bubbles in the topside F region ionosphere near the dawn terminator. A simple analytic model was used which showed how electric fields within the bubbles could be discharged through the conducting sunrise E region. The results showed that the conducting E region could effectively halt the upward bubble rise velocity. This importance of an E region is consistent with our findings in comparing the 2L and 2LE cases.

5. Future Work

The "three layer model" used in this study is simple to be sure, although we believe it adequately describes the qualitative behaviour of ESF plumes in terms of C-shaped structures, westward tilts, and the effects of a background E region. Work toward improving the model and its input is ongoing on several fronts. First, we would like to make the E regions "active", i.e., to allow external forces, such as neutral winds to act on the E region plasma, and to self-consistently solve the continuity equation there. Second, we would like to better resolve the plasma distribution along magnetic field lines by adding more layers to the model to represent plasma between the equatorial plane and the E regions. The total number of layers might be seven or nine. Third, we would like to incorporate more realistic models of electron and neutral density distributions, external electric fields, neutral winds, and chemistry into the models. Sources for this information might be empirical data or models of the type developed by Anderson [1973] and by Forbes and Garrett [1978]. Last, but certainly not least, a continuing effort is being made to keep the numerical techniques used in the code as close to state-of-the-art as possible. A recent advance [Zalesak, 1981] should significantly improve our already quite good, but certainly not perfect, numerical algorithms for solving the continuity equation in the very near future.

ACKNOWLEDGMENT

This work was supported by the Defense Nuclear Agency and the Office of Naval Research. We wish to thank R. Tsunoda for valuable discussions regarding the Kwajalein radar backscatter observations and for providing Figure 12. Also, we wish to thank J.P. McClure for providing Figure 11. Finally, we wish to thank Major Leon Wittwer of DNA for his continued encouragement in the course of this problem.

REFERENCES

Anderson, D.N., A theoretical study of the ionospheric F region equatorial anomaly, I, Theory, Planet. Space Sci., 21, 409, 1973.

Anderson, D.N., and G. Haerendel, The motion of depleted plasma regions in the equatorial ionosphere, J. Geophys. Res., 84, 4251, 1979.

Basu, S., and M.C. Kelley, Review of equatorial scintillation phenomena in light of recent developments in the theory and measurement of equatorial irregularities, J. Atm. Terr. Phys., 39, 1229, 1977.

Boris, J.P., and D.L. Book, Flux-corrected transport, I, Shasta, a transport algorithm that works, J. Comp. Phys., 11, 38, 1973.

Burke, W.J., Plasma bubbles near the dawn terminator in the topside ionosphere, Planet. Space Sci., 27, 1187, 1979.

Doles, J.H., III, N.J. Zabusky, and F.W. Perkins, Deformation and striation of plasma clouds in the ionosphere, 3, Numerical simulations of a multilevel model with recombination chemistry, J. Geophys. Res., 81, 5987, 1976.

Forbes, J.M., and H.B. Garrett, Seasonal-latitudinal structure of the diurnal thermospheric tide, J. Atmos. Sci., 35, 148, 1978.

Hain, K., A non-recursive incomplete Cholesky decomposition method for the solution of linear equations with a sparse matrix, Memo Rept. 4264, Nav. Res. Lab., Washington, D.C., June, 1980.

Heelis, R.A., P.C. Kendall, R.J. Moffett, D.W. Windle, and H. Rishbeth, Electrical coupling of the E- and F-regions and its effect on F-region drifts and winds, Planet. Space Sci., 22, 743, 1974.

Kelley, M.C., M.F. Larsen, C. La Hoz, and J.P. McClure, Gravity wave initiation of equatorial spread F: A case study, J. Geophys. Res. (submitted 1981).

Kershaw, D.S., The incomplete Cholesky-conjugate gradient method for the

iterative solution of systems of linear equations, J. Comp. Phys., 26, 263, 1979.

Kudeki, E., B.G. Fejer, D.T. Farley, and H.M. Ierkic, Interferometer studies of equatorial F region irregularities and drifts, Geophys. Res. Lett., 8, 377, 1981.

Livingston, R.C., Comparison of multifrequency equatorial scintillation: American and Pacific sectors, Radio Sci., 15, 801, 1980.

Lloyd, K.H., and G. Haerendel, Numerical modeling of the drift and deformation of ionospheric plasma clouds and of their interaction with other layers of the ionosphere, J. Geophys. Res., 78, 7387, 1973.

Madala, R.V., An efficient direct solver for separable and nonseparable elliptic equations, Mon. Weather Rev., 106, 1735, 1978.

McClure, J.P., W.B. Hanson, and J.H. Hoffman, Plasma bubbles and irregularities in the equatorial ionosphere, J. Geophys. Res., 82, 2650, 1977.

McDonald, B.E., S.L. Ossakow, S.T. Zalesak, and N.J. Zabusky, Scale sizes and lifetimes of F region plasma cloud striations as determined by the condition of marginal stability, J. Geophys. Res., in press, 1981, also Memo. Rept. 4383, Nav. Res. Lab., Washington, D.C., Nov. 1980.

Ossakow, S.L., and P.K. Chaturvedi, Morphological studies of rising equatorial spread F bubbles, J. Geophys. Res., 83, 2085, 1978.

Ossakow, S.L., S.T. Zalesak, and N.J. Zabusky, Recent results on cleavage, bifurcation, and cascade mechanisms in ionospheric plasma clouds, Memo. Rept. 3579, Nav. Res. Lab., Washington, D.C., Aug. 1977.

Ossakow, S.L., S.T. Zalesak, B.E. McDonald, and P.K. Chaturvedi, Nonlinear equatorial spread F: Dependence on altitude of the F peak and bottomside background electron density gradient scale length, J. Geophys. Res., 84,

17, 1979.

Ott, E., Theory of Rayleigh-Taylor bubbles in the equatorial ionosphere, J. Geophys. Res., 83, 2066, 1978.

Perkins, F.W., and J.H. Doles, III, Velocity shear and the ExB instability, J. Geophys. Res., 80, 211, 1975.

Rishbeth, H., Polarization fields produced by winds in the equatorial F-region, Planet. Space Sci., 19, 357, 1971.

Scannapieco, A.J., and S.L. Ossakow, Nonlinear equatorial spread F, Geophys. Res. Lett., 3, 451, 1976.

Scannapieco, A.J., S.L. Ossakow, D.L. Book, B.E. McDonald, and S.R. Goldman, Conductivity ratio effects on the drift and deformation of F region barium clouds coupled to the E region ionosphere, J. Geophys. Res., 79, 2913, 1974.

Scannapieco, A.J., S.L. Ossakow, S.R. Goldman, and J.M. Pierre, Plasma cloud late time striation spectra, J. Geophys. Res., 81, 6037, 1976.

Tsunoda, R.T., On the spatial relationship of 1-m equatorial spread F irregularities and plasma bubbles, J. Geophys. Res., 85, 185, 1980.

Tsunoda, R.T., Time evolution and dynamics of equatorial backscatter plumes, 1. Growth phase, J. Geophys. Res., 86, 139, 1981.

Tsunoda, R.T., R.C. Livingston, and C.L. Rino, Evidence of a velocity shear in bulk plasma motion associated with the post-sunset rise of the equatorial F layer, Geophys. Res. Lett., submitted, 1981.

Woodman, R.F., and C. La Hoz, Radar observations of F-region equatorial irregularities, J. Geophys. Res., 81, 5447, 1976.

Zabusky, N.J., J.H. Doles, III, and F.W. Perkins, Deformation and striation of plasma clouds in the ionosphere, 2. Numerical simulation of a

nonlinear two-dimensional model, J. Geophys. Res., 78, 711, 1973.

Zalesak, S.T., Fully multidimensional flux-corrected transport algorithms for fluids, J. Comp. Phys., 31, 335, 1979.

Zalesak, S.T., Very high order and pseudospectral flux-corrected transport (FCT) algorithms for conservation laws, to appear in Advances in Computer Methods for Partial Differential Equations-IV (R. Vichnevetsky and R.S. Stepleman, eds.) IMACS, 1981.

Zalesak, S.T., and S.L. Ossakow, Nonlinear equatorial spread F: Spatially large bubbles resulting from large horizontal scale initial perturbations, J. Geophys. Res., 85, 2131, 1980.

Zalesak, S.T., S.L. Ossakow, and P.K. Chaturvedi, An explanation of westward tilts, "fishtails", and "C's" in the equatorial F region ionosphere, Eos Trans. AGU, 61, 1059, 1980.

DISTRIBUTION LIST

DEPARTMENT OF DEFENSE

ASSISTANT SECRETARY OF DEFENSE
COMM, CMD, CONT & INTELL
WASHINGTON, D.C. 20301
    01CY ATTN J. BABCOCK
    01CY ATTN M. EPSTEIN

DIRECTOR
COMMAND CONTROL TECHNICAL CENTER
PENTAGON RM BE 685
WASHINGTON, D.C. 20301
    01CY ATTN C-650
    01CY ATTN C-312 R. MASON

DIRECTOR
DEFENSE ADVANCED RSCH PROJ AGENCY
ARCHITECT BUILDING
1400 WILSON BLVD.
ARLINGTON, VA. 22209
    01CY ATTN NUCLEAR MONITORING RESEARCH
    01CY ATTN STRATEGIC TECH OFFICE

DEFENSE COMMUNICATION ENGINEER CENTER
1860 WIEHLE AVENUE
RESTON, VA. 22090
    01CY ATTN CODE R820
    01CY ATTN CODE R410 JAMES W. MCLEAN
    01CY ATTN CODE R720 J. WORTHINGTON

DIRECTOR
DEFENSE COMMUNICATIONS AGENCY
WASHINGTON, D.C. 20305
    (ADR CNWDI: ATTN CODE 240 FOR)
    01CY ATTN CODE 101B

DEFENSE TECHNICAL INFORMATION CENTER
CAMERON STATION
ALEXANDRIA, VA. 22314
    (12 COPIES IF OPEN PUBLICATION, OTHERWISE 2 COPIES)
    12CY ATTN TC

DIRECTOR
DEFENSE INTELLIGENCE AGENCY
WASHINGTON, D.C. 20301
    01CY ATTN DT-1B
    01CY ATTN DB-4C E. O'FARRELL
    01CY ATTN DIAAP A. WISE
    01CY ATTN DIAST-5
    01CY ATTN DT-1BZ R. MORTON
    01CY ATTN HQ-TR J. STEWART
    01CY ATTN W. WITTIG DC-7D

DIRECTOR
DEFENSE NUCLEAR AGENCY
WASHINGTON, D.C. 20305
    01CY ATTN STVL
    04CY ATTN TITL
    01CY ATTN DDST
    03CY ATTN RAAE

COMMANDER
FIELD COMMAND
DEFENSE NUCLEAR AGENCY
KIRTLAND AFB, NM 87115
    01CY ATTN FCPR

DIRECTOR
INTERSERVICE NUCLEAR WEAPONS SCHOOL
KIRTLAND AFB, NM 87115
    01CY ATTN DOCUMENT CONTROL

JOINT CHIEFS OF STAFF
WASHINGTON, D.C. 20301
    01CY ATTN C3S EVALUATION OFFICE

DIRECTOR
JOINT STRAT TGT PLANNING STAFF
OFFUTT AFB
OMAHA, NB 68113
    01CY ATTN JLTW-2
    01CY ATTN JPST G. GOETZ

CHIEF
LIVERMORE DIVISION FLD COMMAND DNA
DEPARTMENT OF DEFENSE
LAWRENCE LIVERMORE LABORATORY
P. O. BOX 808
LIVERMORE, CA 94550
    01CY ATTN FCPRL

DIRECTOR
NATIONAL SECURITY AGENCY
DEPARTMENT OF DEFENSE
FT. GEORGE G. MEADE, MD 20755
    01CY ATTN JOHN SKILLMAN R52
    01CY ATTN FRANK LEONARD
    01CY ATTN W14 PAT CLARK
    01CY ATTN OLIVER H. BARTLETT W32
    01CY ATTN R5

COMMANDANT
NATO SCHOOL (SHAPE)
APO NEW YORK 09172
    01CY ATTN U.S. DOCUMENTS OFFICER

UNDER SECY OF DEF FOR RSCH & ENGRG
DEPARTMENT OF DEFENSE
WASHINGTON, D.C. 20301
    01CY ATTN STRATEGIC & SPACE SYSTEMS (OS)

WWMCCS SYSTEM ENGINEERING ORG
WASHINGTON, D.C. 20305
    01CY ATTN R. CRAWFORD

COMMANDER/DIRECTOR
ATMOSPHERIC SCIENCES LABORATORY
U.S. ARMY ELECTRONICS COMMAND
WHITE SANDS MISSILE RANGE, NM 88002
    01CY ATTN DELAS-EO F. NILES

DIRECTOR
BMD ADVANCED TECH CTR
HUNTSVILLE OFFICE
P. O. BOX 1500
HUNTSVILLE, AL 35807
    01CY ATTN ATC-T MELVIN T. CAPPS
    01CY ATTN ATC-O W. DAVIES
    01CY ATTN ATC-R DON RUSS

PROGRAM MANAGER
BMD PROGRAM OFFICE
5001 EISENHOWER AVENUE
ALEXANDRIA, VA 22333
    01CY ATTN DACS-BMT J. SHEA

CHIEF C-E SERVICES DIVISION
U.S. ARMY COMMUNICATIONS CMD
PENTAGON RM 1B269
WASHINGTON, D.C. 20310
    01CY ATTN C-E-SERVICES DIVISION

COMMANDER
ERADCOM TECHNICAL SUPPORT ACTIVITY
DEPARTMENT OF THE ARMY
FORT MONMOUTH, N.J. 07703
01CY ATTN DRSEL-NL-RD H. BENNET
01CY ATTN DRSEL-PL-ENV H. BOMKE
01CY ATTN J. E. QUIGLEY

COMMANDER
HARRY DIAMOND LABORATORIES
DEPARTMENT OF THE ARMY
2800 POWDER MILL ROAD
ADELPHI, MD 20783
(CNWDI-INNER ENVELOPE: ATTN: DELHD-RBH)
01CY ATTN DELHD-TI M. WEINER
01CY ATTN DELHD-RB R. WILLIAMS
01CY ATTN DELHD-NP F. WIMENITZ
01CY ATTN DELHD-NP C. MOAZED

COMMANDER
U.S. ARMY COMM-ELEC ENGRG INSTAL AGY
FT. HUACHUCA, AZ 85613
01CY ATTN CCC-EMEO GEORGE LANE

COMMANDER
U.S. ARMY FOREIGN SCIENCE & TECH CTR
220 7TH STREET, NE
CHARLOTTESVILLE, VA 22901
01CY ATTN DRXST-SD
01CY ATTN R. JONES

COMMANDER
U.S. ARMY MATERIEL DEV & READINESS CMD
5001 EISENHOWER AVENUE
ALEXANDRIA, VA 22333
01CY ATTN DRCLDC J. A. BENDER

COMMANDER
U.S. ARMY NUCLEAR AND CHEMICAL AGENCY
7500 BACKLICK ROAD
BLDG 2073
SPRINGFIELD, VA 22150
01CY ATTN LIBRARY

DIRECTOR
U.S. ARMY BALLISTIC RESEARCH LABS
ABERDEEN PROVING GROUND, MD 21005
01CY ATTN TECH LIB EDWARD BAICY

COMMANDER
U.S. ARMY SATCOM AGENCY
FT. MONMOUTH, NJ 07703
01CY ATTN DOCUMENT CONTROL

COMMANDER
U.S. ARMY MISSILE INTELLIGENCE AGENCY
REDSTONE ARSENAL, AL 35809
01CY ATTN JIM GAMBLE

DIRECTOR
U.S. ARMY TRADOC SYSTEMS ANALYSIS ACTIVITY
WHITE SANDS MISSILE RANGE, NM 88002
01CY ATTN ATAA-SA
01CY ATTN TCC/F. PAYAN JR.
01CY ATTN ATAA-TAC LTC J. HESSE

COMMANDER
NAVAL ELECTRONIC SYSTEMS COMMAND
WASHINGTON, D.C. 20360
01CY ATTN NAVALEX 034 T. HUGHES
01CY ATTN PME 117
01CY ATTN PME 117-T
01CY ATTN CODE 5011

COMMANDING OFFICER
NAVAL INTELLIGENCE SUPPORT CTR
4301 SUITLAND ROAD, BLDG. 5
WASHINGTON, D.C. 20390
01CY ATTN MR. DUBBIN STIC 12
01CY ATTN NISC-50
01CY ATTN CODE 5404 J. GALET

COMMANDER
NAVAL OCEAN SYSTEMS CENTER
SAN DIEGO, CA 92152
03CY ATTN CODE 532 W. MOLER
01CY ATTN CODE 0230 C. BAGGETT
01CY ATTN CODE 81 R. EASTMAN

DIRECTOR
NAVAL RESEARCH LABORATORY
WASHINGTON, D.C. 20375
01CY ATTN CODE 4700 T. P. COFFEY (25 CYS IF UN, 1 CY IF CLASS)
01CY ATTN CODE 4701 JACK D. BROWN
01CY ATTN CODE 4780 BRANCH HEAD (150 CYS IF UN, 1 CY IF CLASS)
01CY ATTN CODE 7500
01CY ATTN CODE 7550
01CY ATTN CODE 7580
01CY ATTN CODE 7551
01CY ATTN CODE 7555
01CY ATTN CODE 4730 E. MCLEAN
01CY ATTN CODE 4187

COMMANDER
NAVAL SEA SYSTEMS COMMAND
WASHINGTON, D.C. 20362
01CY ATTN CAPT R. PITKIN

COMMANDER
NAVAL SPACE SURVEILLANCE SYSTEM
DAHLGREN, VA 22448
01CY ATTN CAPT J. H. BURTON

OFFICER-IN-CHARGE
NAVAL SURFACE WEAPONS CENTER
WHITE OAK, SILVER SPRING, MD 20910
01CY ATTN CODE F31

DIRECTOR
STRATEGIC SYSTEMS PROJECT OFFICE
DEPARTMENT OF THE NAVY
WASHINGTON, D.C. 20376
01CY ATTN NSP-2141
01CY ATTN NSSP-2722 FRED WIMBERLY

COMMANDER
NAVAL SURFACE WEAPONS CENTER
DAHLGREN LABORATORY
DAHLGREN, VA 22448
01CY ATTN CODE DF-14 R. BUTLER

OFFICE OF NAVAL RESEARCH
ARLINGTON, VA 22217
01CY ATTN CODE 465
01CY ATTN CODE 461
01CY ATTN CODE 402
01CY ATTN CODE 420
01CY ATTN CODE 421

COMMANDER
AEROSPACE DEFENSE COMMAND/DC
DEPARTMENT OF THE AIR FORCE
ENT AFB, CO 80912
01CY ATTN DC MR. LONG

COMMANDER
AEROSPACE DEFENSE COMMAND/XPD
DEPARTMENT OF THE AIR FORCE
ENT AFB, CO 80912
01CY ATTN XPDQQ
01CY ATTN XP

AIR FORCE GEOPHYSICS LABORATORY
HANSCOM AFB, MA 01731
01CY ATTN OPR HAROLD GARDNER
01CY ATTN OPR-1 JAMES C. ULWICK
01CY ATTN LKB KENNETH S. W. CHAMPION
01CY ATTN OPR ALVA T. STAIR
01CY ATTN PHP JULES AARONS
01CY ATTN PHD JURGEN BUCHAU
01CY ATTN PHD JOHN P. MULLEN

AF WEAPONS LABORATORY
KIRTLAND AFB, NM 87117
01CY ATTN SUL
01CY ATTN CA ARTHUR H. GUENTHER
01CY ATTN NTYC 1LT G. KRAJCI

AFTAC
PATRICK AFB, FL 32925
01CY ATTN TF/MAJ WILEY
01CY ATTN TN

AIR FORCE AVIONICS LABORATORY
WRIGHT-PATTERSON AFB, OH 45433
01CY ATTN AAD WADE HUNT
01CY ATTN AAD ALLEN JOHNSON

DEPUTY CHIEF OF STAFF
RESEARCH, DEVELOPMENT, & ACQ
DEPARTMENT OF THE AIR FORCE
WASHINGTON, D.C. 20330
01CY ATTN AFRDQ

HEADQUARTERS
ELECTRONIC SYSTEMS DIVISION/XR
DEPARTMENT OF THE AIR FORCE
HANSCOM AFB, MA 01731
01CY ATTN XR J. DEAS

HEADQUARTERS
ELECTRONIC SYSTEMS DIVISION/YSEA
DEPARTMENT OF THE AIR FORCE
HANSCOM AFB, MA 01732
01CY ATTN YSEA

HEADQUARTERS
ELECTRONIC SYSTEMS DIVISION/DC
DEPARTMENT OF THE AIR FORCE
HANSCOM AFB, MA 01731
01CY ATTN DCKC MAJ J.C. CLARK

COMMANDER
FOREIGN TECHNOLOGY DIVISION, AFSC
WRIGHT-PATTERSON AFB, OH 45433
01CY ATTN NICD LIBRARY
01CY ATTN ETDP B. BALLARD

COMMANDER
ROME AIR DEVELOPMENT CENTER, AFSC
GRIFFISS AFB, NY 13441
01CY ATTN DOC LIBRARY/TSLD
01CY ATTN OCSE V. COYNE

SAMSO/SZ
POST OFFICE BOX 92960
WORLDWAY POSTAL CENTER
LOS ANGELES, CA 90009
(SPACE DEFENSE SYSTEMS)
01CY ATTN SZJ

STRATEGIC AIR COMMAND/XPFS
OFFUTT AFB, NB 68113
01CY ATTN XPFS MAJ B. STEPHAN
01CY ATTN ADWATE MAJ BRUCE BAUER
01CY ATTN NRT
01CY ATTN DOK CHIEF SCIENTIST

SAMSO/SK
P. O. BOX 92960
WORLDWAY POSTAL CENTER
LOS ANGELES, CA 90009
01CY ATTN SKA (SPACE COMM SYSTEMS) M. CLAVIN

SAMSO/MN
NORTON AFB, CA 92409
(MINUTEMAN)
01CY ATTN MNNL LTC KENNEDY

COMMANDER
ROME AIR DEVELOPMENT CENTER, AFSC
HANSCOM AFB, MA 01731
01CY ATTN EEP A. LORENTZEN

DEPARTMENT OF ENERGY
ALBUQUERQUE OPERATIONS OFFICE
P. O. BOX 5400
ALBUQUERQUE, NM 87115
01CY ATTN DOC CON FOR D. SHERWOOD

DEPARTMENT OF ENERGY
LIBRARY ROOM G-042
WASHINGTON, D.C. 20545
01CY ATTN DOC CON FOR A. LABOWITZ

EG&G, INC.
LOS ALAMOS DIVISION
P. O. BOX 809
LOS ALAMOS, NM 85544
01CY ATTN DOC CON FOR J. BREEDLOVE

UNIVERSITY OF CALIFORNIA
LAWRENCE LIVERMORE LABORATORY
P. O. BOX 808
LIVERMORE, CA 94550
01CY ATTN DOC CON FOR TECH INFO DEPT
01CY ATTN DOC CON FOR L-389 R. OTT
01CY ATTN DOC CON FOR L-31 R. HAGER
01CY ATTN DOC CON FOR L-46 F. SEWARD

LOS ALAMOS SCIENTIFIC LABORATORY
P. O. BOX 1663
LOS ALAMOS, NM 87545
01CY ATTN DOC CON FOR J. WOLCOTT
01CY ATTN DOC CON FOR R. F. TASCHEK
01CY ATTN DOC CON FOR E. JONES
01CY ATTN DOC CON FOR J. MALIK
01CY ATTN DOC CON FOR R. JEFFRIES
01CY ATTN DOC CON FOR J. ZINN
01CY ATTN DOC CON FOR P. KEATON
01CY ATTN DOC CON FOR D. WESTERVELT

SANDIA LABORATORIES
P. O. BOX 5800
ALBUQUERQUE, NM 87115
01CY ATTN DOC CON FOR J. MARTIN
01CY ATTN DOC CON FOR W. BROWN
01CY ATTN DOC CON FOR A. THORNBROUGH
01CY ATTN DOC CON FOR T. WRIGHT
01CY ATTN DOC CON FOR D. DAHLGREN
01CY ATTN DOC CON FOR 3141
01CY ATTN DOC CON FOR SPACE PROJECT DIV

SANDIA LABORATORIES
LIVERMORE LABORATORY
P. O. BOX 969
LIVERMORE, CA 94550
01CY ATTN DOC CON FOR B. MURPHEY
01CY ATTN DOC CON FOR T. COOK

OFFICE OF MILITARY APPLICATION
DEPARTMENT OF ENERGY
WASHINGTON, D.C. 20545
01CY ATTN DOC CON FOR D. GALE

OTHER GOVERNMENT

CENTRAL INTELLIGENCE AGENCY
ATTN RD/SI, RM 5G48, HQ BLDG
WASHINGTON, D.C. 20505
01CY ATTN OSI/PSID RM 5F 19

DEPARTMENT OF COMMERCE
NATIONAL BUREAU OF STANDARDS
WASHINGTON, D.C. 20234
(ALL CORRES: ATTN SEC OFFICER FOR)
01CY ATTN R. MOORE

INSTITUTE FOR TELECOM SCIENCES
NATIONAL TELECOMMUNICATIONS & INFO ADMIN
BOULDER, CO 80303
01CY ATTN A. JEAN (UNCLASS ONLY)
01CY ATTN W. UTLAUT
01CY ATTN D. CROMBIE
01CY ATTN L. BERRY

NATIONAL OCEANIC & ATMOSPHERIC ADMIN
ENVIRONMENTAL RESEARCH LABORATORIES
DEPARTMENT OF COMMERCE
BOULDER, CO 80302
01CY ATTN R. GRUBB
01CY ATTN AERONOMY LAB G. REID

DEPARTMENT OF DEFENSE CONTRACTORS

AEROSPACE CORPORATION
P. O. BOX 92957
LOS ANGELES, CA 90009
01CY ATTN I. GARFUNKEL
01CY ATTN T. SALMI
01CY ATTN V. JOSEPHSON
01CY ATTN S. BOWER
01CY ATTN N. STOCKWELL
01CY ATTN D. OLSEN

ANALYTICAL SYSTEMS ENGINEERING CORP
5 OLD CONCORD ROAD
BURLINGTON, MA 01803
01CY ATTN RADIO SCIENCES

BERKELEY RESEARCH ASSOCIATES, INC.
P. O. BOX 983
BERKELEY, CA 94701
01CY ATTN J. WORKMAN

BOEING COMPANY, THE
P. O. BOX 3707
SEATTLE, WA 98124
01CY ATTN G. KEISTER
01CY ATTN D. MURRAY
01CY ATTN G. HALL
01CY ATTN J. KENNEY

CALIFORNIA AT SAN DIEGO, UNIV OF
P.O. BOX 6049
SAN DIEGO, CA 92106

BROWN ENGINEERING COMPANY, INC.
CUMMINGS RESEARCH PARK
HUNTSVILLE, AL 35807
01CY ATTN ROMEO A. DELIBERIS

CHARLES STARK DRAPER LABORATORY, INC.
555 TECHNOLOGY SQUARE
CAMBRIDGE, MA 02139
01CY ATTN D. B. COX
01CY ATTN J. P. GILMORE

COMSAT LABORATORIES
LINTHICUM ROAD
CLARKSBURG, MD 20734
01CY ATTN G. HYDE

CORNELL UNIVERSITY
DEPARTMENT OF ELECTRICAL ENGINEERING
ITHACA, NY 14850
01CY ATTN D. T. FARLEY JR

ELECTROSPACE SYSTEMS, INC.
BOX 1359
RICHARDSON, TX 75080
01CY ATTN H. LOGSTON
01CY ATTN SECURITY (PAUL PHILLIPS)

ESL INC.
495 JAVA DRIVE
SUNNYVALE, CA 94086
01CY ATTN J. ROBERTS
01CY ATTN JAMES MARSHALL
01CY ATTN C. W. PRETTIE

GENERAL ELECTRIC COMPANY
SPACE DIVISION
VALLEY FORGE SPACE CENTER
GODDARD BLVD KING OF PRUSSIA
P. O. BOX 8555
PHILADELPHIA, PA 19101
01CY ATTN M. H. BORTNER SPACE SCI LAB

GENERAL ELECTRIC COMPANY
P. O. BOX 1122
SYRACUSE, NY 13201
01CY ATTN F. REIBERT

GENERAL ELECTRIC COMPANY
TEMPO-CENTER FOR ADVANCED STUDIES
816 STATE STREET (P.O. DRAWER QQ)
SANTA BARBARA, CA 93102
01CY ATTN DASIAC
01CY ATTN DON CHANDLER
01CY ATTN TOM BARRETT
01CY ATTN TIM STEPHANS
01CY ATTN WARREN S. KNAPP
01CY ATTN WILLIAM MCNAMARA
01CY ATTN B. GAMBILL
01CY ATTN MACK STANTON

GENERAL ELECTRIC TECH SERVICES CO., INC.
HMES
COURT STREET
SYRACUSE, NY 13201
01CY ATTN G. MILLMAN

GENERAL RESEARCH CORPORATION
SANTA BARBARA DIVISION
P. O. BOX 6770
SANTA BARBARA, CA 93111
01CY ATTN JOHN ISE JR
01CY ATTN JOEL GARBARINO

GEOPHYSICAL INSTITUTE
UNIVERSITY OF ALASKA
FAIRBANKS, AK 99701
(ALL CLASS ATTN: SECURITY OFFICER)
01CY ATTN T. N. DAVIS (UNCL ONLY)
01CY ATTN NEAL BROWN (UNCL ONLY)
01CY ATTN TECHNICAL LIBRARY

GTE SYLVANIA, INC.
ELECTRONICS SYSTEMS GRP-EASTERN DIV
77 A STREET
NEEDHAM, MA 02194
01CY ATTN MARSHAL CROSS

ILLINOIS, UNIVERSITY OF
107 COBLE HALL
150 DAVENPORT HOUSE
CHAMPAIGN, IL 61820
(ALL CORRES ATTN DAN MCCLELLAND)
01CY FOR K. YEH

INSTITUTE FOR DEFENSE ANALYSES
400 ARMY-NAVY DRIVE
ARLINGTON, VA 22202
01CY ATTN J. M. AEIN
01CY ATTN ERNEST BAUER
01CY ATTN HANS WOLFHARD
01CY ATTN JOEL BENGSTON

HSS, INC.
2 ALFRED CIRCLE
BEDFORD, MA 01730
01CY ATTN DONALD HANSEN

INTL TEL & TELEGRAPH CORPORATION
500 WASHINGTON AVENUE
NUTLEY, NJ 07110
01CY ATTN TECHNICAL LIBRARY

JAYCOR
1401 CAMINO DEL MAR
DEL MAR, CA 92014
01CY ATTN S. R. GOLDMAN

JOHNS HOPKINS UNIVERSITY
APPLIED PHYSICS LABORATORY
JOHNS HOPKINS ROAD
LAUREL, MD 20810
01CY ATTN DOCUMENT LIBRARIAN
01CY ATTN THOMAS POTEMRA
01CY ATTN JOHN DASSOULAS

LOCKHEED MISSILES & SPACE CO INC
P. O. BOX 504
SUNNYVALE, CA 94088
01CY ATTN DEPT 60-12
01CY ATTN D. R. CHURCHILL

LOCKHEED MISSILES AND SPACE CO INC
3251 HANOVER STREET
PALO ALTO, CA 94304
01CY ATTN MARTIN WALT DEPT 52-10
01CY ATTN RICHARD G. JOHNSON DEPT 52-12
01CY ATTN W. L. IMHOF DEPT 52-12

KAMAN SCIENCES CORP
P. O. BOX 7463
COLORADO SPRINGS, CO 80933
01CY ATTN T. MEAGHER

LINKABIT CORP
10453 ROSELLE
SAN DIEGO, CA 92121
01CY ATTN IRWIN JACOBS

M.I.T. LINCOLN LABORATORY
P. O. BOX 73
LEXINGTON, MA 02173
01CY ATTN DAVID M. TOWLE
01CY ATTN P. WALDRON
01CY ATTN L. LOUGHLIN
01CY ATTN D. CLARK

MARTIN MARIETTA CORP
ORLANDO DIVISION
P. O. BOX 5837
ORLANDO, FL 32805
01CY ATTN R. HEFFNER

PHYSICAL DYNAMICS INC.
P. O. BOX 3027
BELLEVUE, WA 98009
01CY ATTN E. J. FREMOUW

PHYSICAL DYNAMICS INC.
P. O. BOX 10367
OAKLAND, CA. 94610
ATTN: A. THOMSON

R & D ASSOCIATES
P. O. BOX 9695
MARINA DEL REY, CA 90291
01CY ATTN FORREST GILMORE
01CY ATTN BRYAN GABBARD
01CY ATTN WILLIAM B. WRIGHT JR
01CY ATTN ROBERT F. LELEVIER
01CY ATTN WILLIAM J. KARZAS
01CY ATTN H. ORY
01CY ATTN C. MACDONALD
01CY ATTN R. TURCO

RAND CORPORATION, THE
1700 MAIN STREET
SANTA MONICA, CA 90406
01CY ATTN CULLEN CRAIN
01CY ATTN ED BEDROZIAN

RIVERSIDE RESEARCH INSTITUTE
80 WEST END AVENUE
NEW YORK, NY 10023
01CY ATTN VINCE TRAPANI

SCIENCE APPLICATIONS, INC.
P. O. BOX 2351
LA JOLLA, CA 92038
01CY ATTN LEWIS M. LINSON
01CY ATTN DANIEL A. HAMLIN
01CY ATTN D. SACHS
01CY ATTN E. A. STRAKER
01CY ATTN CURTIS A. SMITH
01CY ATTN JACK MCDOUGALL

RAYTHEON CO.
528 BOSTON POST ROAD
SUDBURY, MA 01776
01CY ATTN BARBARA ADAMS

SCIENCE APPLICATIONS, INC.
1710 GOODRIDGE DR.
MCLEAN, VA 22102
ATTN: J. COCKAYNE

LOCKHEED MISSILE & SPACE CO., INC.
HUNTSVILLE RESEARCH & ENGR. CTR.
4800 BRADFORD DRIVE
HUNTSVILLE, ALABAMA 35807
ATTN: DALE H. DAVIS

MCDONNELL DOUGLAS CORPORATION
5301 BOLSA AVENUE
HUNTINGTON BEACH, CA 92647
01CY ATTN N. HARRIS
01CY ATTN J. MOULE
01CY ATTN GEORGE MROZ
01CY ATTN W. OLSON
01CY ATTN R. W. HALPRIN
01CY ATTN TECHNICAL LIBRARY SERVICES

MISSION RESEARCH CORPORATION
735 STATE STREET
SANTA BARBARA, CA 93101
01CY ATTN P. FISCHER
01CY ATTN W. F. CREVIER
01CY ATTN STEVEN L. GUTSCHE
01CY ATTN D. SAPPENFIELD
01CY ATTN R. BOGUSCH
01CY ATTN R. HENDRICK
01CY ATTN RALPH KILB
01CY ATTN DAVE SOWLE
01CY ATTN F. FAJEN
01CY ATTN M. SCHEIBE
01CY ATTN CONRAD L. LONGMIRE
01CY ATTN WARREN A. SCHLUETER

MITRE CORPORATION, THE
P. O. BOX 208
BEDFORD, MA 01730
01CY ATTN JOHN MORGANSTERN
01CY ATTN G. HARDING
01CY ATTN C. E. CALLAHAN

MITRE CORP
WESTGATE RESEARCH PARK
1820 DOLLY MADISON BLVD
MCLEAN, VA 22101
01CY ATTN W. HALL
01CY ATTN W. FOSTER

PACIFIC-SIERRA RESEARCH CORP
1456 CLOVERFIELD BLVD.
SANTA MONICA, CA 90404
01CY ATTN E. C. FIELD JR

PENNSYLVANIA STATE UNIVERSITY
IONOSPHERE RESEARCH LAB
318 ELECTRICAL ENGINEERING EAST
UNIVERSITY PARK, PA 16802
(NO CLASSIFIED TO THIS ADDRESS)
01CY ATTN IONOSPHERIC RESEARCH LAB

PHOTOMETRICS, INC.
442 MARRETT ROAD
LEXINGTON, MA 02173
01CY ATTN IRVING L. KOFSKY

TECHNOLOGY INTERNATIONAL CORP
75 WIGGINS AVENUE
BEDFORD, MA 01730
01CY ATTN W. P. BOQUIST

TRW DEFENSE & SPACE SYS GROUP
ONE SPACE PARK
REDONDO BEACH, CA 90278
01CY ATTN R. K. PLEBUCH
01CY ATTN S. ALTSCHULER
01CY ATTN D. DEE

SRI INTERNATIONAL
333 RAVENSWOOD AVENUE
MENLO PARK, CA 94025
01CY ATTN DONALD NEILSON
01CY ATTN ALAN BURNS
01CY ATTN G. SMITH
01CY ATTN L. L. COBB
01CY ATTN DAVID A. JOHNSON
01CY ATTN WALTER G. CHESNUT
01CY ATTN CHARLES L. RINO
01CY ATTN WALTER JAYE
01CY ATTN M. BARON
01CY ATTN RAY L. LEADABRAND
01CY ATTN G. CARPENTER
01CY ATTN G. PRICE
01CY ATTN J. PETERSON
01CY ATTN R. HAKE, JR.
01CY ATTN V. GONZALES
01CY ATTN D. MCDANIEL

IONOSPHERIC MODELING DISTRIBUTION LIST
UNCLASSIFIED ONLY

Please distribute one copy to each of the following people:

Naval Research Laboratory
Washington, D.C. 20375

Dr. P. Mange - Code 4101
Dr. R. Meier - Code 4141
Dr. E. Szuszczewicz - Code 4187
Dr. J. Goodman - Code 4180

Science Applications, Inc.
1250 Prospect Plaza
La Jolla, California 92037

Dr. D. A. Hamlin
Dr. L. Linson
Dr. D. Sachs

Director of Space and Environmental
Laboratory, NOAA
Boulder, Colorado 80302

Dr. A. Glenn Jean
Dr. G. W. Adams
Dr. D. N. Anderson
Dr. K. Davies
Dr. R. F. Donnelly

A. F. Geophysics Laboratory
L. G. Hanscom Field
Bedford, Mass. 01730

Dr. T. Elkins
Dr. W. Swider
Mrs. R. Sagalyn
Dr. J. M. Forbes
Dr. T. J. Keneshea
Dr. J. Aarons

Office of Naval Research
800 North Quincy Street
Arlington, Virginia 22217

Dr. H. Mullaney

Commander
Naval Electronics Laboratory Center
San Diego, California 92152

Mr. R. Rose - Code 5321

U.S. Army Aberdeen Research and
Development Center
Ballistic Research Laboratory
Aberdeen, MD

Dr. J. Heimerl

Commander
Naval Air Systems Command
Department of the Navy
Washington, D.C. 20360

Dr. T. Czuba

Harvard University
Harvard Square
Cambridge, Mass. 02138

Dr. M. B. McElroy
Dr. R. Lindzen

Pennsylvania State University
University Park, Pennsylvania 16802

Dr. J. S. Nisbet
Dr. P. R. Rohrbaugh
Dr. L. A. Carpenter
Dr. M. Lee
Dr. R. Divany
Dr. P. Bennett
Dr. E. Klevans

University of California, Los Angeles
405 Hillgard Avenue
Los Angeles, California 90024

Dr. F. V. Coroniti
Dr. C. Kennel

University of California, Berkeley
Berkeley, California 94720

Dr. M. Hudson

Utah State University
4th N. and 8th Streets
Logan, Utah 84322

Dr. P. M. Banks
Dr. R. Harris
Dr. K. Baker

Cornell University
Ithaca, New York 14850

Dr. W. E. Swartz
Dr. R. Sudan
Dr. D. Farley
Dr. M. Kelley

NASA
Goddard Space Flight Center
Greenbelt, Maryland 20771

Dr. S. Chandra
Dr. K. Maeda
Dr. R.F. Benson

Princeton University
Plasma Physics Laboratory
Princeton, New Jersey 08540

Dr. F. Perkins
Dr. E. Frieman

Institute for Defense Analysis
400 Army/Navy Drive
Arlington, Virginia 22202

Dr. E. Bauer

University of Maryland
College Park, MD 20742

Dr. K. Papadopoulos
Dr. E. Ott

University of Pittsburgh
Pittsburgh, Pa. 15261

Dr. N. Zabusky
Dr. M. Biondi

Defense Documentation Center
Cameron Station
Alexandria, VA 22314

(12 copies if open publication
otherwise 2 copies)

12CY Attn TC

University of California
Los Alamos Scientific Laboratory
J-10, MS-664
Los Alamos, New Mexico 87545

M. Pongracz
D. Simons
G. Barasch
L. Duncan

Massachusetts Institute of Technology
Plasma Fusion Center
Library, NW16-262
Cambridge, MA 02139